

# Dynamics of a buoyant pulsating bubble near two crossed walls

Li, Shi Min; Liu, Yun Long; Wang, Qianxi; Zhang, A. Man

DOI:  
[10.1063/5.0057594](https://doi.org/10.1063/5.0057594)

License:  
None: All rights reserved

*Document Version*  
Publisher's PDF, also known as Version of record

*Citation for published version (Harvard):*  
Li, SM, Liu, YL, Wang, Q & Zhang, AM 2021, 'Dynamics of a buoyant pulsating bubble near two crossed walls', *Physics of Fluids*, vol. 33, no. 7, 073310. <https://doi.org/10.1063/5.0057594>

[Link to publication on Research at Birmingham portal](#)

## General rights

Unless a licence is specified above, all rights (including copyright and moral rights) in this document are retained by the authors and/or the copyright holders. The express permission of the copyright holder must be obtained for any use of this material other than for purposes permitted by law.

- Users may freely distribute the URL that is used to identify this publication.
- Users may download and/or print one copy of the publication from the University of Birmingham research portal for the purpose of private study or non-commercial research.
- User may use extracts from the document in line with the concept of 'fair dealing' under the Copyright, Designs and Patents Act 1988 (?)
- Users may not further distribute the material nor use it for the purposes of commercial gain.

Where a licence is displayed above, please note the terms and conditions of the licence govern your use of this document.

When citing, please reference the published version.

## Take down policy

While the University of Birmingham exercises care and attention in making items available there are rare occasions when an item has been uploaded in error or has been deemed to be commercially or otherwise sensitive.

If you believe that this is the case for this document, please contact [UBIRA@lists.bham.ac.uk](mailto:UBIRA@lists.bham.ac.uk) providing details and we will remove access to the work immediately and investigate.

# Dynamics of a buoyant pulsating bubble near two crossed walls

Cite as: Phys. Fluids **33**, 073310 (2021); <https://doi.org/10.1063/5.0057594>

Submitted: 22 May 2021 • Accepted: 28 June 2021 • Published Online: 15 July 2021

 Shi-Min Li (李世民),  Yun-Long Liu (刘云龙),  Qianxi Wang, et al.



View Online



Export Citation



CrossMark

## ARTICLES YOU MAY BE INTERESTED IN

[Numerical study of the shock wave and pressure induced by single bubble collapse near planar solid wall](#)

Physics of Fluids **33**, 073311 (2021); <https://doi.org/10.1063/5.0055727>

[Interaction of two out-of-phase underwater explosion bubbles](#)

Physics of Fluids **33**, 106103 (2021); <https://doi.org/10.1063/5.0064164>

[The acoustic pressure generated by the cavitation bubble expansion and collapse near a rigid wall](#)

Physics of Fluids **33**, 032118 (2021); <https://doi.org/10.1063/5.0043822>

Physics of Fluids

SPECIAL TOPIC: Flow and Acoustics of Unmanned Vehicles

Submit Today!

# Dynamics of a buoyant pulsating bubble near two crossed walls

Cite as: Phys. Fluids **33**, 073310 (2021); doi: [10.1063/5.0057594](https://doi.org/10.1063/5.0057594)

Submitted: 22 May 2021 · Accepted: 28 June 2021 ·

Published Online: 15 July 2021



View Online



Export Citation



CrossMark

Shi-Min Li (李世民),<sup>1</sup> Yun-Long Liu (刘云龙),<sup>1,a)</sup> Qianxi Wang,<sup>1,2</sup> and A-Man Zhang (张阿漫)<sup>1</sup>

## AFFILIATIONS

<sup>1</sup>College of Shipbuilding Engineering, Harbin Engineering University, Harbin 150001, People's Republic of China

<sup>2</sup>School of Mathematics, University of Birmingham, Edgbaston, Birmingham B15 2TT, United Kingdom

<sup>a)</sup>Author to whom correspondence should be addressed: [yunlong\\_liu@hrbeu.edu.cn](mailto:yunlong_liu@hrbeu.edu.cn)

## ABSTRACT

The dynamics of a buoyant pulsating bubble near two crossed perpendicular rigid boundaries (a horizontal and a vertical wall) are studied using the boundary element method combined with the method of mirror images. The Kelvin impulse and the elastic mesh velocity method are used to calculate the direction and volume of the liquid jet generated during bubble collapse. The numerical results show good agreement with experiments. An increase in buoyancy causes a local high-pressure zone at the root of the jet to move toward the bottom of the bubble, causing the jet to rotate upward toward the vertical wall. At a certain position, with the change in buoyancy, the dimensionless bubble volume at the instant of jet impact reaches a minimum when the jet direction is horizontal, with a peak in the dimensionless jet velocity occurring. A comprehensive parametric study of jet characteristics, including jet direction, velocity, and relative volume (the volume ratio of the jet to the bubble at the instant of jet impact), is carried out in terms of buoyancy and the standoff distances to the two walls. The Blake criterion can be used to judge whether a bubble jet is pointing obliquely upward or downward, provided that it deviates significantly from the horizontal direction. Depending on the buoyancy, the jet characteristics at different standoff distances are found to exhibit three distinct patterns of behavior. Finally, we discuss the changes in the jet velocity and relative volume as the buoyancy is varied.

Published under an exclusive license by AIP Publishing. <https://doi.org/10.1063/5.0057594>

## I. INTRODUCTION

The dynamics of bubbles near walls are relevant to cavitation erosion,<sup>1–4</sup> marine prospecting,<sup>5,6</sup> ultrasonic cleaning of mechanical components,<sup>7–9</sup> and watercourse dredging.<sup>10</sup> As the bubble length scale increases, the mass of liquid displaced by bubble pulsations becomes greater, and thus, the effects of buoyancy effect become significant. The study of buoyant bubbles (with obvious scale effects) is a crucial aspect of bubble dynamics, since the effects of buoyancy play a vital role in many processes, including resource exploration,<sup>11,12</sup> submarine volcanic eruptions,<sup>13–15</sup> and underwater explosions.<sup>16–22</sup> A deeper understanding of the mechanisms involved in the behavior of buoyant bubbles would help in harnessing their advantages for some applications as well as preventing their adverse effects in others.

One of the most important and interesting features of bubble dynamics near a rigid wall is the creation of high-speed liquid jets.<sup>1,23–31</sup> These jets point toward the wall in the case of small-scale bubbles and interact with the flow field close to the wall. In the late stage of bubble collapse, they may even hit the wall. The energy contained in these jets and their directivity toward the wall are fundamental causes of cavitation erosion of mechanical components.<sup>32,33</sup> Bubble

dynamics near a single rigid wall have been thoroughly studied in recent decades.<sup>1,34–42</sup> Blake *et al.*<sup>37</sup> discussed the combined influence of buoyancy and a rigid wall on the jet direction, and the resulting “Blake criterion” is widely used to determine the jet direction in the case of a bubble above a rigid wall. In most cases of practical interest, more than one wall is present, and therefore, bubble dynamics near multiple walls have received much attention in recent years.<sup>43–48</sup> However, most of these studies have focused on aspects of bubble dynamics relevant to cavitation, medicine, and ultrasonic cleaning, and have ignored the effects of buoyancy. For a bubble subject to buoyancy, the jet may not necessarily point toward the wall, and it is important to take this into account, since the characteristics of the jet depend on its direction. In our previous work,<sup>43,49–51</sup> we have shown that the jet direction near complex boundaries changes significantly when the effect of buoyancy is taken into account. However, those studies focused primarily on the analysis of specific cases and the description of physical phenomena. There has been a lack of systematic studies of the jet direction, velocity, and volume near complex boundaries, owing to the complicated parameters and difficult calculations required when, for example, computing the inclined jet volume.

In this study, we concentrate on bubble dynamics near two mutually perpendicular semi-infinite rigid walls, which represent one of the most basic types of complex boundaries and correspond to the physical scenario encountered in ultrasonic descaling, mechanical draft tubes, and underwater explosions near a shore. Determination of the physical mechanisms involved in this relatively simple physical model will provide a basis for the solution of more complex problems in the future. Because large-scale bubble experiments such as large-equivalent-charge underwater explosions are expensive and environmentally destructive, we choose to study bubble dynamics through numerical simulations. We adopt the boundary element method (BEM) because of its high accuracy and efficiency. The volume of the inclined jet is calculated by placing a spherical topology externally using the “elastic mesh velocity” method. The relative jet volume is defined and studied because it can better represent the range of influence of the jet impact relative to the bubble pulsations. An underwater explosion experiment is conducted to validate the numerical algorithm. A parametric study is then conducted on the jet direction, velocity, and relative volume. In a dimensionless framework, we present the spatial distribution of jet characteristics under four typical buoyancy effects. The variation in jet characteristics with distance is divided into three distinct categories based on the Blake criterion. For a bubble at a fixed distance, the peak jet velocity appears when the jet direction is horizontal.

## II. NUMERICAL MODEL

### A. Physical model and numerical methods

Figure 1 shows the physical model adopted in this study, with the two pink planes representing the semi-infinite bottom and the sidewall and the blue ball representing the initial bubble. The coordinate system is set up at the bubble centroid, with the  $z$  axis pointing in the opposite direction to gravity and the  $y$  axis pointing away from the sidewall. There are two distance parameters involved: the distance  $d_b$  between

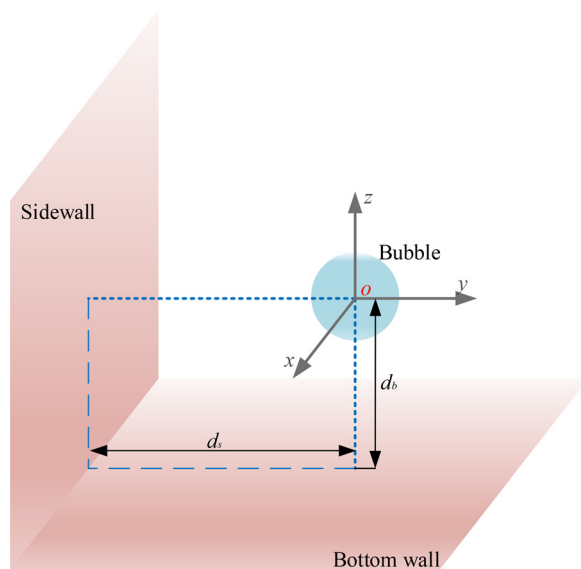


FIG. 1. Coordinate system and parameter definitions.

the initial bubble and the bottom, and the distance  $d_s$  between the initial bubble and the sidewall. Since the two parameters are asymmetric under the action of buoyancy, they are considered separately instead of being treated equally.

The viscosity, rotation, and compressibility of the fluid can all be ignored,<sup>46,52,53</sup> and so we can solve the following boundary integral equation<sup>11,54</sup> to simulate the pulsation and jetting behavior of the bubble:

$$\kappa(\mathbf{p})\phi(\mathbf{p}) + \iint_s \frac{\partial G(\mathbf{p}, \mathbf{q})}{\partial n(\mathbf{q})} \varphi(\mathbf{q}) ds = \iint_s G(\mathbf{p}, \mathbf{q}) \frac{\partial \phi(\mathbf{q})}{\partial n(\mathbf{q})} ds, \quad (1)$$

where  $\phi$  is the velocity potential of the fluid flow,  $G$  is the Green function,  $s$  is the area of the boundary surface of the fluid domain,  $\kappa$  is the solid angle,  $\partial/\partial n$  is the normal derivative at the nodes on the bubble surface, and  $\mathbf{p}$  and  $\mathbf{q}$  are, respectively, the source and integration points on the bubble surface. By discretizing the bubble surface using triangular meshes and assuming that  $\phi$  is known at each time step, we can transform Eq. (1) into a linear equation system<sup>55,56</sup> with  $N$  unknowns of  $\partial\phi/\partial n$  (where  $N$  denotes the number of nodes). By solving this equation system, we can obtain the normal velocities of the nodes on the bubble surface.

Because the physical process is unsteady, the bubble surface velocity potential needs to be updated<sup>40,57,58</sup> using the Bernoulli equation

$$\frac{d\phi}{dt} = \frac{1}{2} |\nabla \phi|^2 - \frac{1}{\rho} \left[ p_0 \left( \frac{V_0}{V} \right)^\eta - p_\infty \right] - gz, \quad (2)$$

where  $p_\infty$  is the hydrostatic pressure at the initial bubble center,  $\rho$  is the liquid density,  $g$  is the acceleration due to gravity,  $p_0(V_0/V)^\eta$  is the internal pressure of the bubble calculated based on the adiabatic law,<sup>53</sup>  $p_0$  is the initial internal pressure, and  $\eta$  is the specific heat ratio [taken as 1.25 for a bubble generated by an explosion of trinitrotoluene (TNT) explosive].

For the rigid walls, the method of mirror images<sup>51,59</sup> is adopted to account for its influence instead of directly discretizing, which has better efficiency and accuracy. In Eq. (1), the Green function is taken as  $1/|\mathbf{p} - \mathbf{q}|$ . Under the assumption of an infinite and impenetrable rigid wall, an exactly similar image bubble is present symmetrically on the other side of the wall, and the Green function then becomes  $1/|\mathbf{p} - \mathbf{q}| + 1/|\mathbf{p} - \mathbf{q}_0|$ , where  $\mathbf{q}_0$  is the image of  $\mathbf{q}$  with respect to the wall. Here, the Green function needs to satisfy the boundary conditions on both walls simultaneously. Three bubbles need to be added to satisfy the impenetrability of the two perpendicular walls at the same time. Hence, the Green function becomes

$$G(\mathbf{p}, \mathbf{q}) = \frac{1}{|\mathbf{p} - \mathbf{q}|} + \frac{1}{|\mathbf{p} - \mathbf{q}_1|} + \frac{1}{|\mathbf{p} - \mathbf{q}_2|} + \frac{1}{|\mathbf{p} - \mathbf{q}_3|}, \quad (3)$$

where  $\mathbf{q}_1$  and  $\mathbf{q}$  are symmetrical about the bottom wall,  $\mathbf{q}_2$  and  $\mathbf{q}$  are symmetrical about the sidewall, and  $\mathbf{q}_3$  and  $\mathbf{q}$  are symmetrical about the line of intersection of the two walls.

In the simulation, we employ the density potential method (DPM) to ensure the quality of meshes and prevent meshes from being too dense or sparse in local areas.<sup>53</sup> The pulsation and jetting of the bubble can be accurately captured by solving Eqs. (1)–(3), while the pressure in the flow field needs to be obtained separately as

$$p = p_\infty + \rho \left( -\frac{1}{2} |\nabla \phi|^2 - gz - \frac{\partial \phi}{\partial t} \right). \quad (4)$$

The indirect BEM is employed to solve for the velocity of the flow field,  $\nabla \phi$ . This method is well known in potential flow theory, and so we will not describe it here in detail. It is worth mentioning, however, that we use the acceleration potential<sup>60</sup>  $\dot{\phi} = \partial \phi / \partial t$  to avoid direct calculation of the time difference [the fourth term on the right-hand side of Eq. (4)] when solving for the pressure in the flow field. It can be seen in Eq. (1) that the acceleration potential  $\dot{\phi} = \partial \phi / \partial t$  also satisfies the boundary integral equation, and its boundary conditions on the bubble surface can also be derived from Eq. (4). Therefore, we can use Eqs. (1)–(3) to solve for the pressure and velocity of the flow field at any time.

To control the stability of numerical simulations, the time step needs to be limited by controlling the change of velocity potential and ensure that the time step does not exceed a specific value

$$\Delta t = \left\{ \frac{C_0}{\Delta \phi}, \frac{\Delta \phi}{\max(|d\phi/dt|)} \right\}, \quad (5)$$

where  $C_0$  is the minimum length of grid lines and  $\Delta \phi$  is the variation value of velocity potential between two adjacent time steps.

## B. Dimensionless system

Dimensionless physical quantities are adopted to make the result of the study universal. The distance, density, and pressure can be characterized by the maximum bubble radius  $R_m$ , the liquid density  $\rho$ , and the hydrostatic pressure  $p_\infty$  of the initial bubble. In this way, in the subsequent numerical calculations, the dimensionless maximum radius of the bubble is 1.0, which is convenient when presenting the corresponding physical mechanisms. The dimensionless reference quantities of velocity, velocity potential, and time are then  $\sqrt{p_\infty/\rho}$ ,  $R_m \sqrt{p_\infty/\rho}$ , and  $R_m \sqrt{\rho/p_\infty}$ , respectively. We employ a widely used dimensionless coefficient to characterize the effect of buoyancy, namely, the buoyancy parameter  $\delta$ , which is the reciprocal of the Froude number<sup>35,61</sup> and characterizes the relative magnitude of gravity and inertial force

$$\delta = \sqrt{\frac{\rho g R_m}{p_\infty}}. \quad (6)$$

The greater  $\delta$  means the bigger scale of the bubble, so the pressure gradient around the bubble in the vertical direction is more significant with increasing  $\delta$ .

In addition, we need to define two dimensionless distance parameters, namely, the dimensionless distances between the bubble and the bottom and sidewall, respectively,

$$\gamma_b = \frac{d_b}{R_m}, \quad \gamma_s = \frac{d_s}{R_m}. \quad (7)$$

In the dimensionless system, Eqs. (2) and (4) can be rewritten as

$$\frac{d\phi'}{\partial t'} = 1 + \frac{1}{2} |\nabla \phi'|^2 - \varepsilon \left( \frac{V_0'}{V'} \right)^\eta - \delta^2 z', \quad (8)$$

$$P' = 1 - \frac{1}{2} |\nabla \phi'|^2 - \delta^2 z' - \frac{\partial \phi'}{\partial t'}, \quad (9)$$

where the dimensionless quantities are indicated by a prime, and  $\varepsilon$  is the strength parameter of the bubble (the dimensionless initial internal pressure).

## C. Calculation of jet direction and jet volume

The direction of the jet from a bubble can be quantified by a well-known quantity, the Kelvin impulse<sup>52,62</sup>  $\mathbf{I}(t)$ , which is given in dimensionless form by

$$\mathbf{I}(t) = \int_s \phi' \mathbf{n} \, ds. \quad (10)$$

The ratio of the component of the Kelvin impulse in the  $z$  direction,  $I_z$ , to that in the  $y$  direction,  $I_y$ , is used to calculate the jet angle  $\alpha$  as follows:

$$\alpha = \arctan \left( \frac{I_z}{I_y} \right). \quad (11)$$

To facilitate subsequent quantitative studies, the jet angle is taken to be zero when the jet is directed toward the sidewall, and the sign follows the right-hand rule with respect to the opposite direction of  $x$  axis.

The jet volume is also an essential feature of a bubble jet. In an axisymmetric configuration, the liquid jet and a horizontal line at its root of the jet together form a closed surface, and the jet volume (i.e., the volume of the liquid domain included in the concave part of the bubble surface at the instant of jet impact) can be determined by calculating the area of this closed surface.<sup>12</sup> However, in three-dimensional cases, the complex topology of the inclined jet makes it very difficult to calculate the jet volume directly. In this situation, we calculate the jet volume through the following procedure:

1. At the instant of jet impact, a spherical bubble with the same topology as the original bubble is created, with the centroid of the original bubble as its center and the distance between the center and the node farthest from the center as its radius.
2. The nodes on the new bubble update their positions when they are located outside the jetting bubble; otherwise, they remain static. The updating velocity of the nodes on the new bubble, that is, the elastic mesh velocity, is given by

$$\mathbf{v} = \begin{cases} \frac{1}{n} \sum_{i=1}^n (\mathbf{r}_i - \mathbf{r}), & \mathbf{v} \Delta t \cdot \mathbf{n} \leq (\mathbf{r} - \mathbf{r}_c) \cdot \mathbf{n}, \\ 0, & \mathbf{v} \Delta t \cdot \mathbf{n} > (\mathbf{r} - \mathbf{r}_c) \cdot \mathbf{n}, \end{cases} \quad (12)$$

where  $n$  denotes the number of nodes in a circle around the updating node,  $\mathbf{r}_i$  and  $\mathbf{r}$  are the location vectors of the surrounding nodes and the updating node,  $\mathbf{r}_c$  is the position vector of the node closest to the updated node on the original bubble,  $\mathbf{n}$  is the normal vector of the node closest to the updated node, and  $\Delta t$  is the updating time step. The time step should be chosen to ensure that the displacement of the bubble nodes at each time step is less than the minimum distance between nodes:

$$|\mathbf{v}| \Delta t < \frac{1}{2} \min |\mathbf{r}_i - \mathbf{r}_j|, \quad i, j = 1, 2, \dots, N. \quad (13)$$

3. When the difference between the bubble volume before and after each time step is less than a minimum value (the selection of this



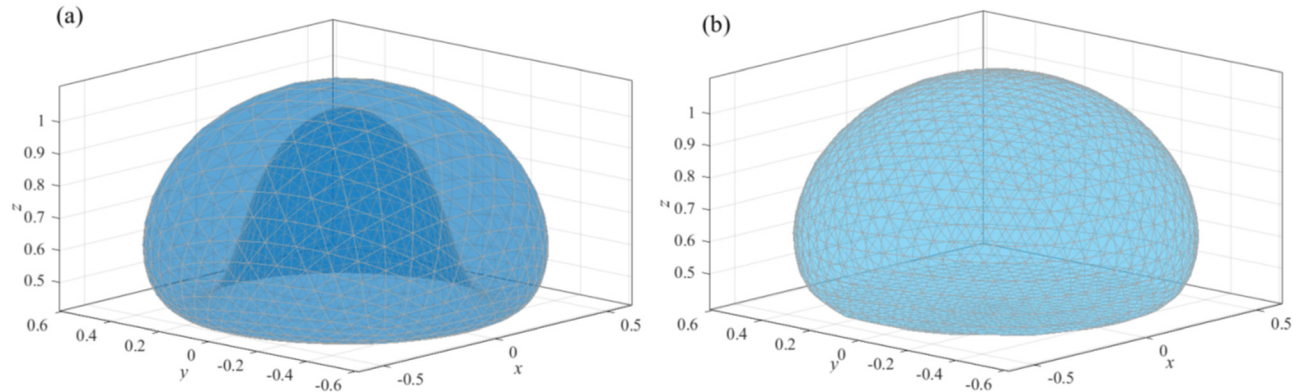


**FIG. 2.** Jetting bubble and new bubble. The bubble is discretized into 2880 triangular elements by 1442 nodes. (a) Bubble profile at the instant of jet impact with  $\delta$  of 0.5 ( $\varepsilon = 100$ ,  $\eta = 1.4$ ). (b) New bubble profile after updating the positions of nodes.

minimum value is relatively arbitrary, as long as it ensures that the new bubble tightly wraps around the jetting bubble; here, we select 0.000 01, the updating is stopped. The jet volume  $V_{\text{jet}}$  is then calculated by subtracting the volume of the original bubble from that of the new bubble.

Figure 2(a) presents the bubble shape with  $\delta = 0.5$  in the free field at the instant of jet impact, and Fig. 2(b) shows the shape of the new bubble after the above procedure. The profile and size of the new bubble are in good agreement with those of the jetting bubble, except that the lower part of the bubble is flat rather than recessed inward. Using the method of Li *et al.*,<sup>12</sup> we calculate the jet volume for the same case in the axisymmetric configuration. The error between the two results is less than 0.3%, indicating that the reliability of the above procedure is high.

The relative jet volume  $V_{\text{jet}}/V$  (where  $V$  is the bubble volume at the instant of jet impact) is actually a more significant physical quantity than the jet volume  $V_{\text{jet}}$ . A larger relative jet volume means that the jet contacts a larger proportion of the bubble surface during bubble collapse, and hence, the radiated pressure range<sup>41,63–65</sup> caused by the jet impact increases relative to the pulsation load of the bubble. We focus below on the changes in the relative jet volume for different buoyancies and distances from the walls.

### III. VALIDATION OF NUMERICAL MODEL

To evaluate the feasibility of the numerical model, we carried out an underwater explosion experiment in a  $4 \times 4 \times 4 \text{ m}^3$  water tank. Eight experiments are conducted, including explosions in a free field (Fig. 3) and near another bubble (Fig. 4). Eleven grams of hexogen (RDX) explosive was used to produce a bubble with a maximum radius of 36 cm (the buoyancy parameter  $\delta = 0.19$ ). In the experiment, it is challenging to ensure complete rigidity of the walls. Therefore, we arranged two equivalent explosives horizontally, resulting in the formation of an infinite rigid wall at the vertical bisector of the line connecting the two charges. A high-speed camera (Phantom V710) was used to record the evolution of the bubble at a frame rate of 7000 frames/s. In Fig. 4, the numerically simulated and experimentally measured bubble profiles are compared at several typical instants in the first cycle. The equivalent rigid wall is 50 cm away from the initial bubble ( $\gamma_s = 1.71$ ). In the numerical simulation, we need to select a suitable

initial condition for bubble pulsation to match the experimental bubble scale and period. The initial radius  $R_0$  and inner pressure  $\varepsilon$  can be estimated through the traditional Rayleigh–Plesset equation.<sup>66,67</sup> The choice of  $\varepsilon$  is relatively arbitrary, because it has a weak influence on the bubble dynamics between values of 20 and 500,<sup>68</sup> and therefore, in the subsequent calculations, it is reasonable that  $\varepsilon$  is taken as 100. The reference length in the numerical simulation is the maximum radius of the bubble, which can be obtained from an empirical formula:<sup>69</sup>

$$R_m = A \left( \frac{W}{H + 10} \right)^{1/3}, \quad (14)$$

where  $W$  and  $H$  are the weight and depth of explosives, respectively.

For TNT explosives,  $A$  is taken as 3.38. Before experimenting, we fitted the equivalent coefficient of RDX explosives relative to TNT explosives by carrying out experiments in a free field, as shown in Fig. 3. The weight of RDX we use is equivalent to about 1.319 times TNT explosives in terms of  $R_m$ . Hence,  $R_m$  in the numerical simulation can be calculated as 36.2 cm.  $\eta$  is set to 1.6 because the pulsation period

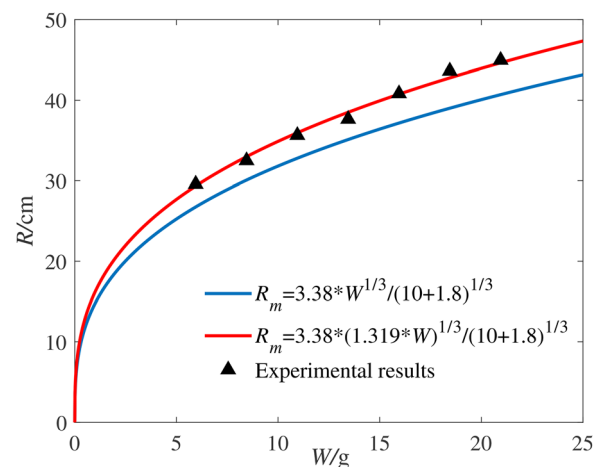


**FIG. 3.** Equivalent coefficient of RDX relative to TNT explosives in terms of the maximum bubble radius.

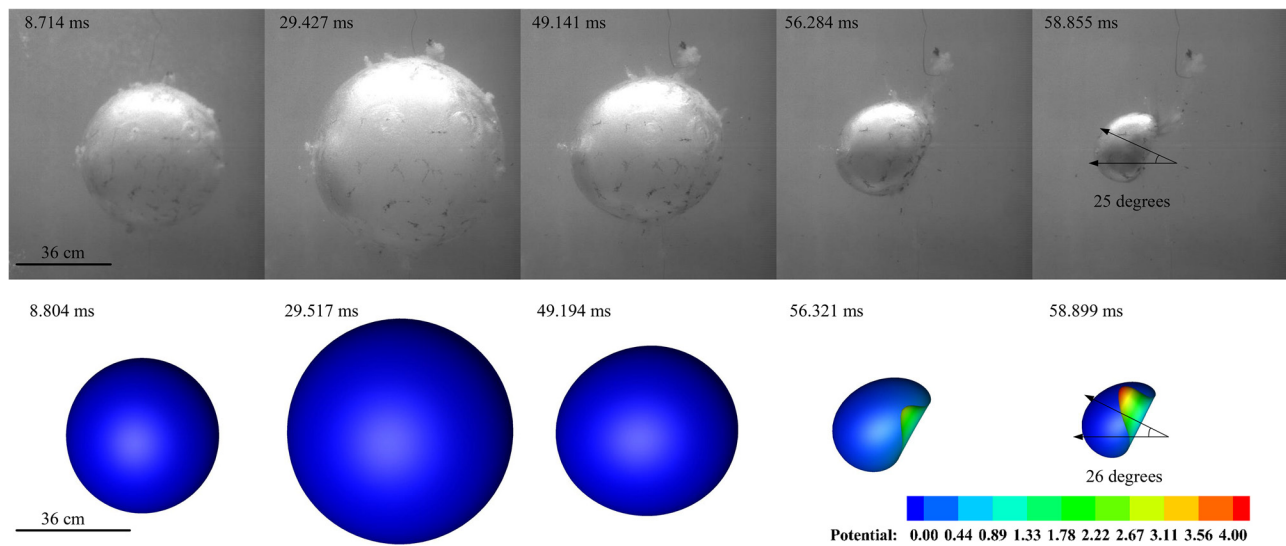


**FIG. 4.** Experimental and corresponding numerical results. The time corresponding to each frame is marked in the upper left corner. The solid black line indicates the length scale in the lower left corner of the first frame. The color on the bubble surface in the numerical results shows the distribution of the velocity potential: the velocity potential of the bubble surface can roughly represent the velocity distribution on the bubble surface; the value of the velocity potential represents the normal velocity of the nodes on the bubble surface; the negative velocity potential means that the bubble expands outward and the positive one means inward contraction; and the gradient of velocity potential along the bubble wall denotes the tangential velocity.

in the simulation agrees with the experimental value under this  $\eta$  through trials.

The bubble maintains spherical expansion at  $t < 29.427$  ms and is affected by buoyancy and the equivalent rigid wall simultaneously during its collapse. A diagonally upward liquid jet forms and tends to impact the opposite bubble surface at  $t = 58.855$  ms. The jet direction is calculated to be  $26^\circ$  according to Eq. (11), which is consistent with the result based on the measurement of the bubble profile in the experimental image ( $25^\circ$ ). Note that we define the jet direction by the Kelvin impulse, characterizing the movement trend of bubbles. The direction of the calculated jet is consistent with jet velocity rather than the intuitive direction of the liquid column formed by the jet, as shown in Fig. 5. Hence, the calculated jet direction is different from the direction of the liquid column, as shown in Figs. 4 and 5.

#### IV. ANALYSIS OF RESULTS

##### A. Physical phenomena

We first investigate the bubble dynamics when the initial bubble is closer to the bottom wall ( $\gamma_b < \gamma_s$ ). Figure 6 shows the bubble profile and its surrounding pressure and velocity fields for  $\gamma_b = 1.5$ ,  $\gamma_s = 2$ , and different buoyancy parameters  $\delta = 0, 0.2, 0.4$ , and  $0.6$ . The bottom row displays the bubble shape in the top view (for  $\delta = 0$  and  $0.2$ ) and bottom view (for  $\delta = 0.4$  and  $0.6$ ) at the instant of jet impact. During the bubble expansion stage (not shown), the fluid between the bubble and boundaries is confined, while the fluid far from the boundary is relatively accessible, and as a result, the velocity field around the bubble is not symmetrical as the bubble expands to its maximum volume (first row). The fluid between the bubble and the nearer wall is squeezed more severely during the bubble expansion stage and then flows to the far wall or the free side. Therefore, at  $\delta = 0$  and  $0.2$ , owing to the relatively weak buoyancy effect, at the instant at which the

bubble reaches its maximum volume, the fluid close to the sidewall moves clockwise, while the fluid far away from the sidewall flows counterclockwise. As the buoyancy effect is enhanced ( $\delta = 0.4$  and  $0.6$ ), the difference in the vertical hydrostatic pressure becomes greater, and the fluid below the bubble tends to flow upward, causing the fluid close to the sidewall to move counterclockwise, while the fluid far

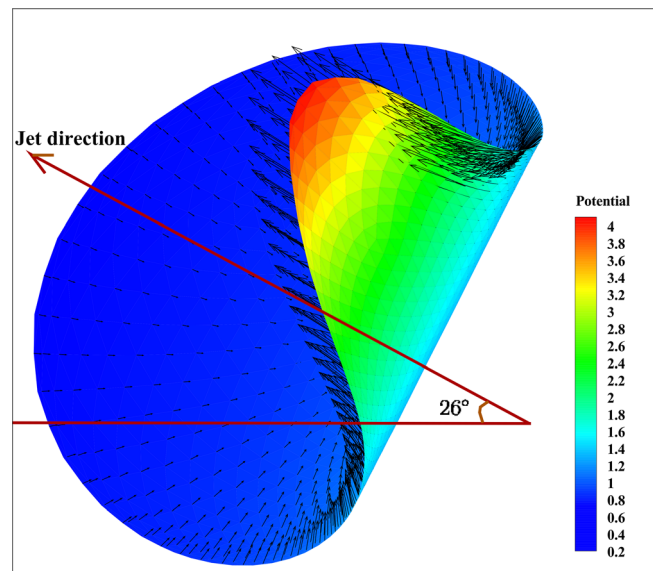


**FIG. 5.** Velocity distribution of the bubble surface ( $t = 58.899$  ms). The velocity vectors of nodes on the bubble surface are plotted in the form of arrows. The color on the bubble surface shows the distribution of the velocity potential.

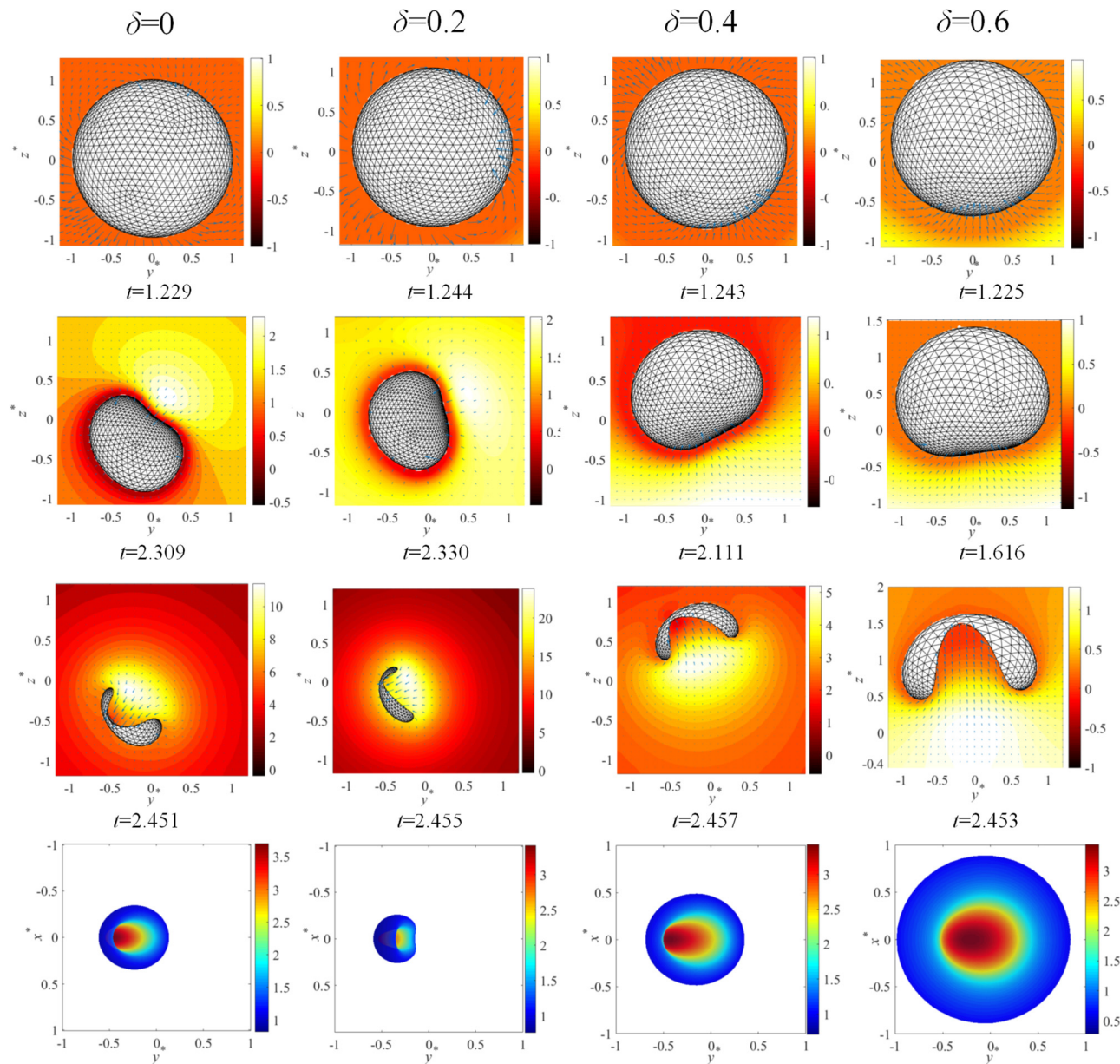


**FIG. 6.** Bubble profile at typical instants of collapse for  $\gamma_b = 1.5$ ,  $\gamma_s = 2.0$ , and four different buoyancy parameters. In the side views in the top three rows, the pressure and velocity fields are given in the form of cloud diagrams and vector arrows, respectively. The bottom row shows the top ( $\delta = 0$  and  $0.2$ ) and bottom ( $\delta = 0.4$  and  $0.6$ ) views at the instant of jet impact, with the colors on the bubble surface representing the distribution of the velocity potential. The initial bubble internal pressure  $\varepsilon = 100$ , and the initial bubble radius  $R_0 = 0.16$ .

away from the sidewall flows clockwise. The asymmetry of the velocity field leads directly to distortion of the bubble during its contraction stage. The fluid velocity becomes very low as the two counter-moving fluid flows converge, resulting in a sharp local pressure increase (second row). Driven by this local high-pressure zone, the bubble surface opposite the nearer wall and far away from the other wall collapses faster, and hence, a liquid jet is formed and impacts the opposite bubble surface (third row).

As  $\delta$  increases, the local high-pressure zone at the root of the jet rotates clockwise relative to the bubble, and its area gradually increases. From the top and bottom views of the bubble shape in the final row of Fig. 6, it can be seen that both the horizontal and vertical spans become wider for  $\delta = 0.4$  and  $0.6$  in a clear manifestation of the increasingly dominant effect of buoyancy. The bubble volume at the instant of jet impact is smallest when  $\delta = 0.2$ , which is related to the relative strengths of the effects of the two walls and buoyancy. For



$\delta = 0.2$ , the liquid jet is directed almost toward the sidewall, and two oppositely moving fluid flows converge at the vertical center relative to the bubble. Compared with other values of  $\delta$ , this convergence occurs later, resulting in a larger collapse velocity of the bubble surface when the jet is formed, and the bubble volume at the instant of jet impact is smaller. These physical characteristics can be attributed to the influence of the Bjerknes force.<sup>35</sup> In the absence of buoyancy, the formation of the liquid jet results from an uneven pressure field caused by the boundaries (the so-called secondary Bjerknes force, which is related to the effects of the sidewall and bottom wall in this study). When the effect of buoyancy is strong, the pressure gradient of the flow field surrounding the bubble is the leading cause of the formation of the liquid jet (the so-called primary Bjerknes force).

Figure 7 illustrates the evolution of the bubble equivalent radius, the Kelvin impulse in the  $y$  and  $z$  directions, and the jet velocity (the velocity of the jet tip, i.e., the node on the liquid jet closest to the opposite bubble surface at jet impact). Four cases are considered, and the parameters of each case are the same as those shown in Fig. 6. For larger  $\delta$ , the bubble becomes larger in volume at the instant of jet impact, and the corresponding pulsation frequency decreases. The Kelvin impulse in the  $y$  direction remains negative throughout this period owing to the sidewall effect, and its rate of changeover time is larger at the beginning of bubble expansion and toward the end of bubble collapse.  $I_y$  becomes larger during bubble collapse for  $\delta = 0.6$

than for other values of  $\delta$ , because the wide upward jet weakens the trend of bubble movement toward the sidewall.  $I_z$  increases with increasing  $\delta$ , as does its rate of increase, owing to the more significant buoyancy effect. The buoyancy effect of the left two cases is weak, and bubbles are greatly affected by the Bjerknes force of the bottom surface in the vertical direction, so the jet tends to point diagonally downward. For the right two cases, bubbles are mainly driven by buoyancy in the vertical direction, so the jet is directed obliquely upwards toward the wall. The difference in bubble migration and jet direction is reflected in the  $z$  Kelvin impulse. Because the bubble has a smaller volume during its collapse, the speed of collapse is greater. Hence, the jet velocity at the instant of jet impact is highest for  $\delta = 0.2$ . With a significant buoyancy effect ( $\delta = 0.4$  and  $0.6$ ), a larger  $\delta$  corresponds to a lower jet velocity, because the bubble has a larger volume at the instant of jet impact.

Figure 8 shows the bubble shapes and the surrounding pressure and velocity fields for  $\delta = 0, 0.2, 0.4$ , and  $0.6$  when the initial bubble is closer to the sidewall ( $\gamma_b = 2$  and  $\gamma_s = 1.5$ ). The pressure and velocity fields have similar features to those in Fig. 6, but the local high-pressure zones are more inclined to the sidewall during bubble collapse, because the bubble is affected more strongly by the secondary Bjerknes force from the sidewall. For  $\delta = 0.2$ , the wider liquid jet points toward the sidewall, reflecting the more substantial secondary Bjerknes force in the horizontal direction. Figure 9 shows the bubble

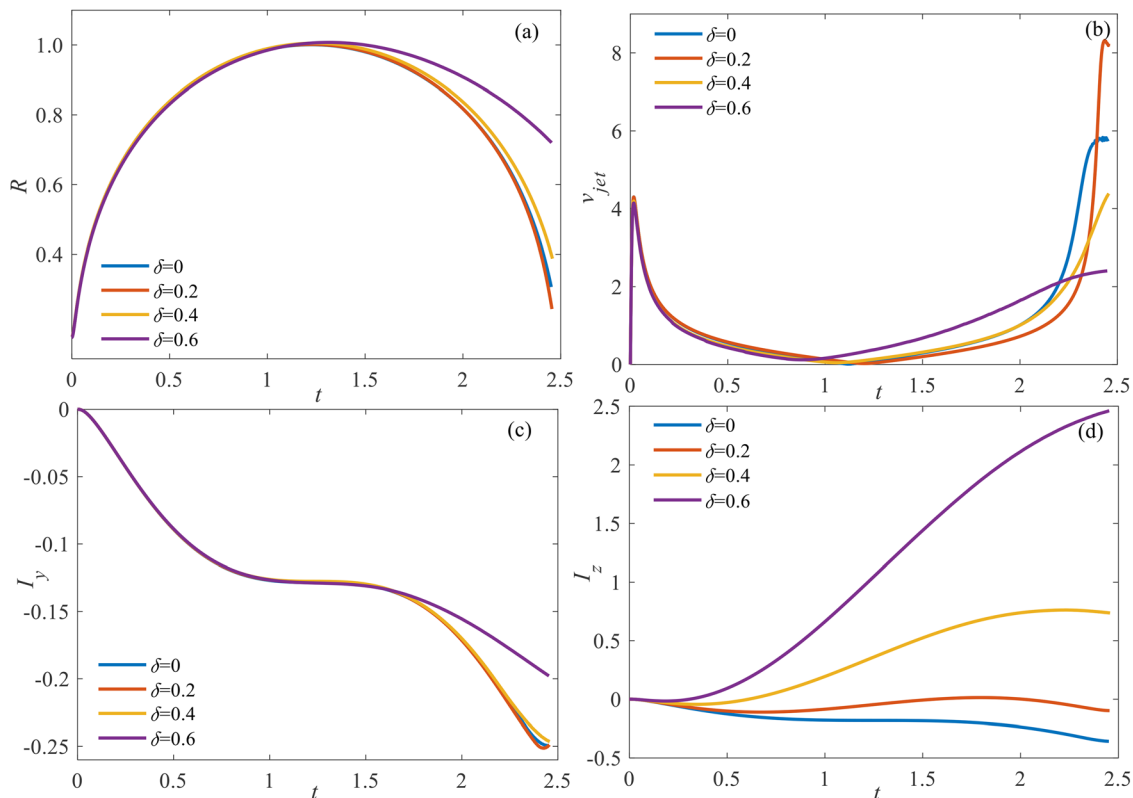


**FIG. 7.** Evolution of the bubble equivalent radius, jet velocity, and Kelvin impulse in the  $y$  and  $z$  directions for the four cases shown in Fig. 6. (a) Bubble radius. (b) Jet velocity. (c) Kelvin impulse in the  $y$  direction. (d) Kelvin impulse in the  $z$  direction.

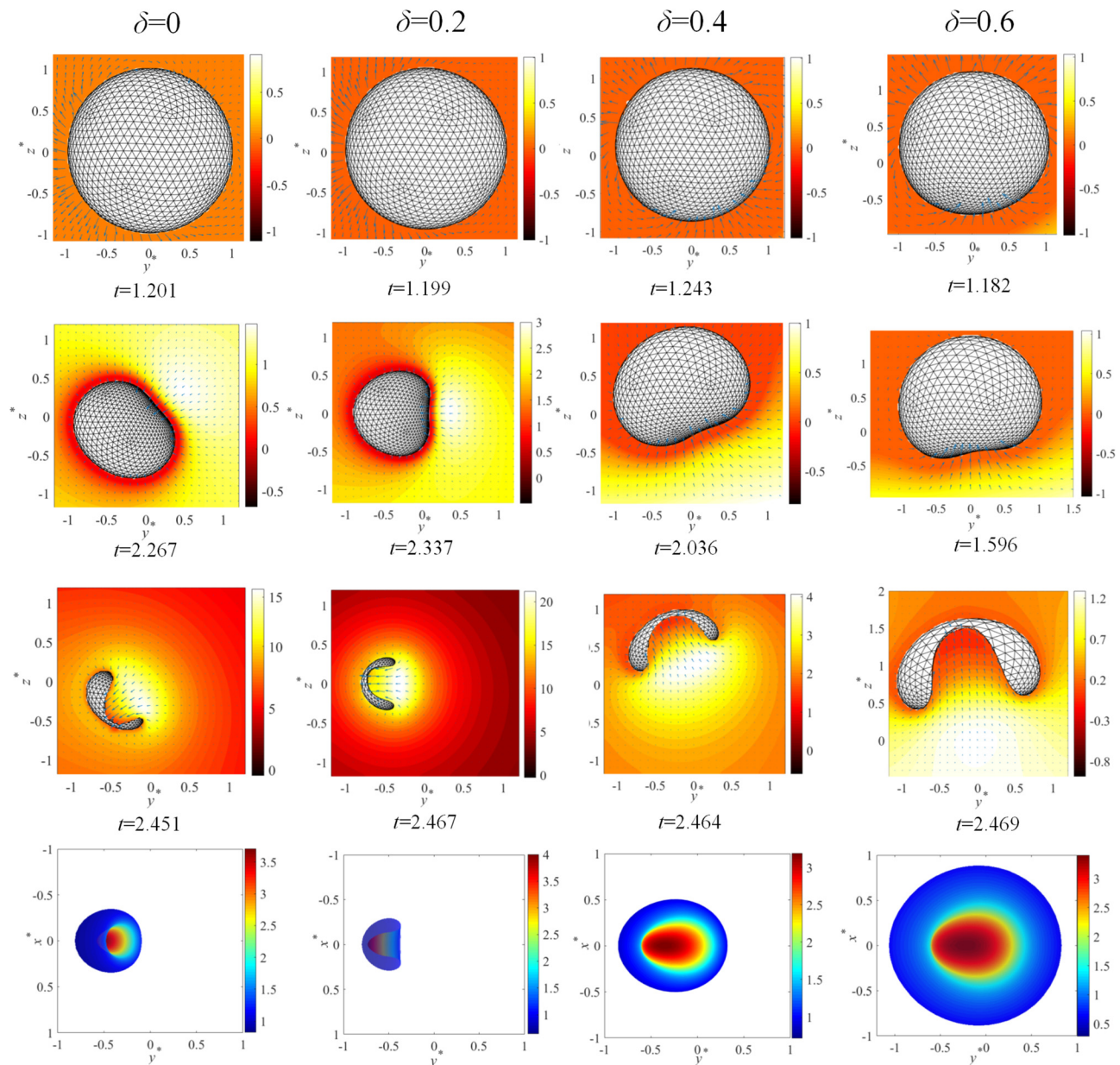


**FIG. 8.** Bubble profile at typical instants of collapse for  $\gamma_b = 2.0$ ,  $\gamma_s = 1.5$ , and four different buoyancy parameters. In the side views in the top three rows, the pressure and velocity fields are given in the form of cloud diagrams and vector arrows, respectively. The bottom row shows the top ( $\delta = 0$  and  $0.2$ ) and bottom ( $\delta = 0.4$  and  $0.6$ ) views at the instant of jet impact, with the colors on the bubble surface representing the distribution of the velocity potential. The initial bubble internal pressure is  $\varepsilon = 100$ , and the initial bubble radius is  $R_0 = 0.16$ .

radius, the Kelvin impulse in the  $y$  and  $z$  directions, and the jet velocity over time for the four cases shown in Fig. 8. The pulsation frequency and change in Kelvin impulse with  $\delta$  are similar to those shown in Fig. 7. The velocity of the jet tip is equal to the bubble pulsation velocity in the first half-cycle and is dominated by the liquid jet in the second half-cycle. A noteworthy feature is that at  $\delta = 0.4$  and  $0.6$ , the change in jet velocity with respect to time becomes more gentle in

the final stage of bubble collapse, whereas the jet velocity always increases during bubble collapse in the case shown in Fig. 7. This can be explained by the fact that because the bubble is farther from the bottom, the buoyancy effect in the vertical direction is less offset by the secondary Bjerknes force from the bottom wall, and the amplitude of the upward bubble migration increases; consequently, the upward flowing fluid is more dispersed at the root of the jet.

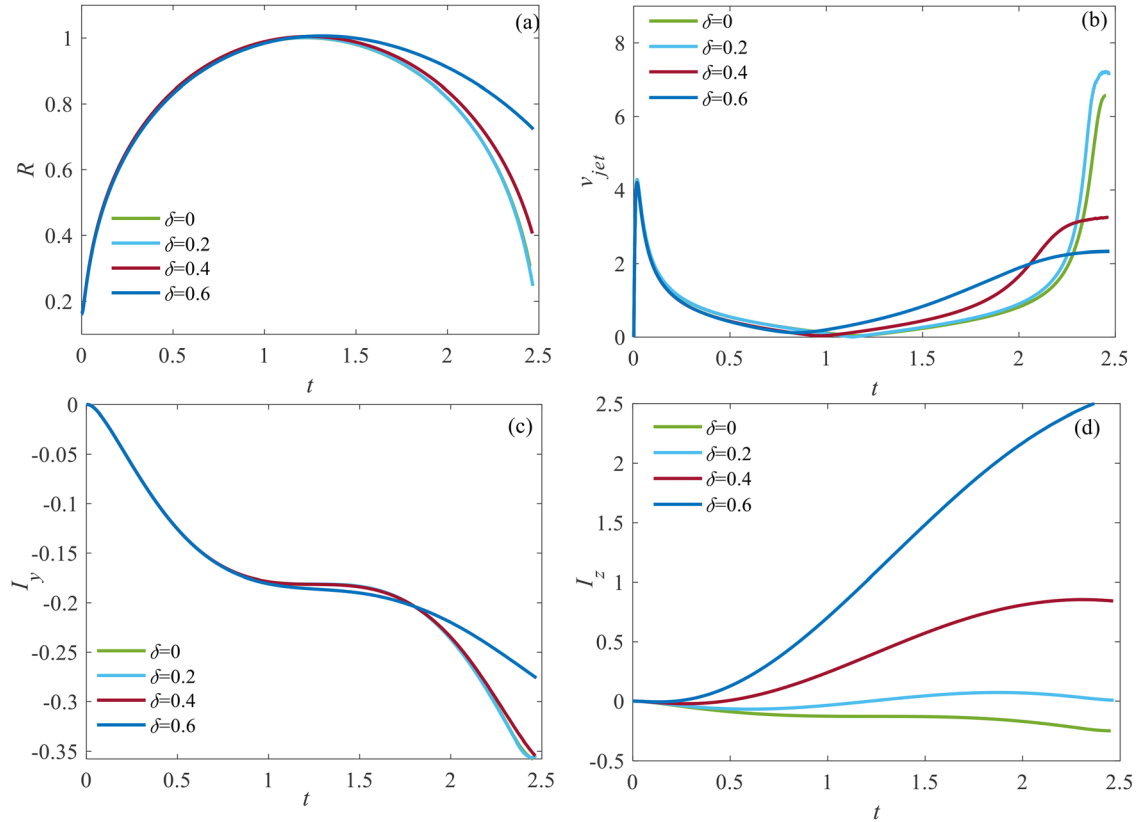


**FIG. 9.** Evolution of the bubble equivalent radius, jet velocity, and Kelvin impulse in the  $y$  and  $z$  directions for the four cases shown in Fig. 8. (a) Bubble radius. (b) Jet velocity. (c) Kelvin impulse in the  $y$  direction. (d) Kelvin impulse in the  $z$  direction.

## B. Jet characteristics for typical buoyancy parameters

In this subsection, the jet characteristics for four values of the buoyancy parameter  $\delta = 0, 0.2, 0.4$ , and  $0.6$  are studied in terms of the standoff distance parameters. Related results<sup>37,49</sup> have shown that as the dimensionless distance from the walls exceeds 6, the influence of the walls becomes negligible. Therefore, there is no need to consider values of  $\gamma_b$  and  $\gamma_s$  greater than 6. In addition, when the bubble is close to walls, the resulting strong effects of the wall are beyond the scope of this study, and so only values of  $\gamma_b$  and  $\gamma_s$  greater than 1 will be considered, to ensure that the bubble does not touch the walls, at least in the first period.

### 1. Blake criterion

A spherical bubble is subjected to two forces when located above an infinite rigid wall: buoyancy and Bjerknes force from the bottom wall. The resultant force<sup>37</sup> can be expressed as

$$F_z(t) = -\frac{\rho M(t)^2}{16\pi d_b^2} + \frac{4}{3}\rho g \pi R^3(t), \quad (15)$$

where  $M(t)$  is the intensity of the source when the bubble is regarded as a point source ( $M(t) = \pm 4\pi\sqrt{\frac{2}{3}}\frac{P_\infty}{\rho}R^2\sqrt{\frac{R_m^3}{R^3} - 1}$ ).

The impulse of the bubble when it shrinks to the minimum volume can be obtained by integrating Eq. (15) and taking the integration interval as twice the Rayleigh collapse time  $T_0$ <sup>70</sup> ( $T_0 = 0.915$ ),

$$I = \int_0^{2T_0} F_z(t) dt = \frac{2\sqrt{6}\pi}{9} R_m^3 \sqrt{\rho P_\infty} \left( 2\delta^2 B\left(\frac{11}{6}, \frac{1}{2}\right) - \frac{1}{\gamma_b^2} B\left(\frac{7}{6}, \frac{3}{2}\right) \right), \quad (16)$$

where  $B$  is the Beta function.

According to Eq. (16), as  $\gamma_b \delta \approx 0.44$ , the impulse of the bubble is zero; that is, the bubble tends to stay still. When the product  $\gamma_b \delta > 0.44$ , the effect of buoyancy is dominant, and when  $\gamma_b \delta < 0.44$ , the effect of the bottom wall is dominant.

### 2. $\delta = 0$

We present the distribution of the jet characteristics near two perpendicular walls in the absence of buoyancy. The direction, velocity, volume, and relative volume of the liquid jet for 40 cases with different values of  $\gamma_b$  and  $\gamma_s$  are shown in Fig. 10. The liquid jet always points to the nearer wall and is inclined to the other wall. Therefore, the jet angle is always negative and increases with  $\gamma_b$  but decreases with  $\gamma_s$ . The jet velocity increases with both  $\gamma_b$  and  $\gamma_s$  simultaneously, since the weaker coupling effect between the bubble and the rigid wall

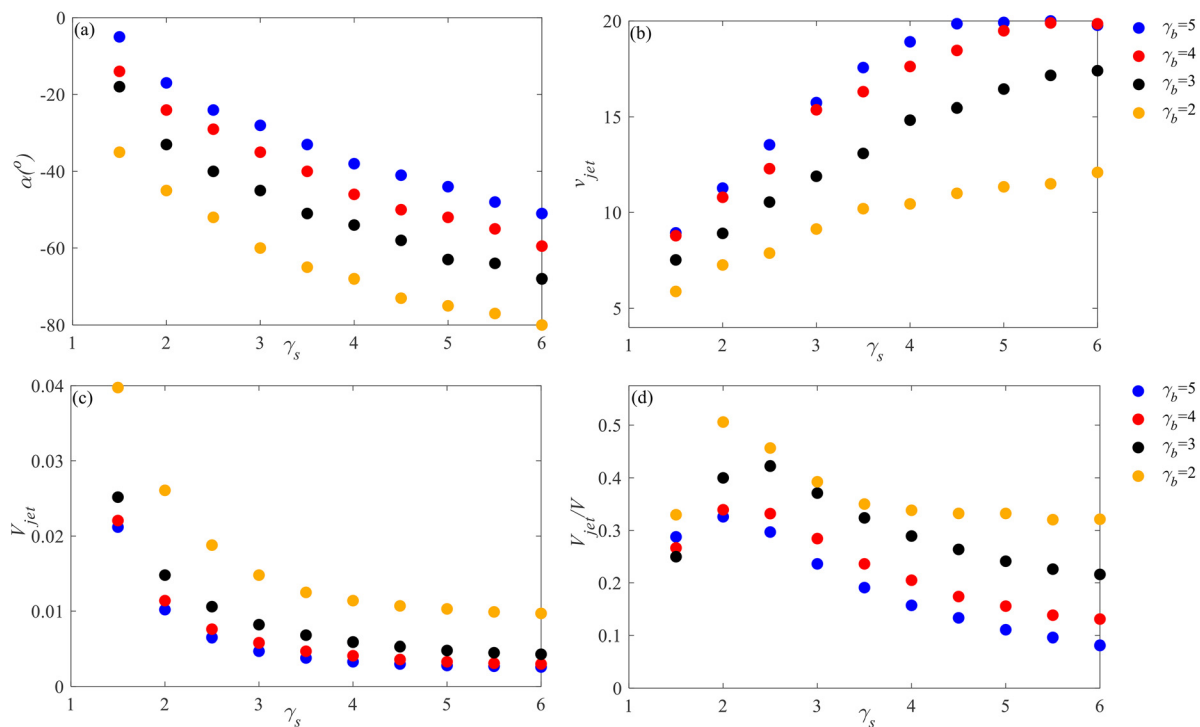


**FIG. 10.** Changes in the jet angle, velocity, volume, and relative volume with respect to  $\gamma_s$  for  $\delta = 0$  and  $\gamma_b = 2, 3, 4$ , and  $5$ . (a) Jet direction. (b) Jet velocity. (c) Jet volume. (d) Relative jet volume.

causes the bubble to have a smaller volume and a greater collapse velocity at the instant of jet impact, which is consistent with related numerical and experimental analyses.<sup>44,59,71</sup> As  $\gamma_b$  or  $\gamma_s$  increases, the jet volume decreases owing to the smaller bubble volume at the instant of jet impact, and it eventually converges to a stable value. The relative jet volume first increases and then decreases with increasing  $\gamma_s$ , with the peak occurring at the bisector of the corner at  $\gamma_s = \gamma_b = 2$ . The two walls simultaneously restrict bubble pulsation with equal effects at the bisector, causing a greater extent of fluid far from the walls to flow inward. Similar features have been discussed in detail previously.<sup>43</sup> As  $\gamma_b$  increases, there is no longer a peak at the bisector, because the bubble pulsation becomes closer to that in a free field, and the jet volume and relative volume are both smaller than near the walls owing to the weak secondary Bjerknes force. Therefore, a peak in the relative jet volume only occurs in the corner bisector as the initial bubble approaches the corner, when the standoff distance is around 2.

Although there is no buoyancy effect in these cases, the discussion of the phenomena for cases with  $\delta = 0$  is still valid, since the same physical mechanisms related to the Bjerknes force apply provided that the effect of buoyancy is weaker than that of the bottom wall. Based on the Blake criterion, if  $\gamma_b \delta < 0.44$  in the entire region under consideration (i.e.,  $\delta < 0.073$ ), then the discussion without buoyancy is still applicable.

### 3. $\delta = 0.2$

Figure 11 displays the jet direction, velocity, volume, and relative volume for 50 cases with different values of  $\gamma_b$  and  $\gamma_s$ , for  $\delta = 0.2$

(equivalent to the bubble produced by the explosion of approximately 25 g TNT<sup>72,73</sup>). The jet angle is negative when  $\gamma_b = 1.5$  and positive when  $\gamma_b = 2, 3, 4$ , and  $5$ , because the effect of buoyancy offsets that of the bottom wall to varying degrees for different values of  $\gamma_b$ . For  $\gamma_b = 2$ , there is a little deviation of the liquid jet from the horizontal plane ( $|\alpha| < 20^\circ$ ). This means that the secondary Bjerknes force and buoyancy effect almost cancel each other out, whereas the bottom wall has a dominant effect in the vertical direction at  $\gamma_b = 1.5$ , and the effect of buoyancy dominates at  $\gamma_b = 3, 4$ , and  $5$ . The upward or downward deflection of the jet direction conforms to the Blake criterion,<sup>37</sup> except for  $\gamma_b = 2$ . As the effect of buoyancy is weaker than that of the bottom wall, the changes in the jet characteristics are similar to those in the absence of buoyancy, but with the effect of buoyancy weakening the influence of the bottom wall on these characteristics. Hence, when the jet is directed obliquely downward ( $\alpha < 0^\circ$ ), its volume decreases more rapidly with  $\gamma_s$ , and its velocity increases more rapidly with  $\gamma_s$  than in the case of an obliquely upward jet. Furthermore, although the jet velocity is low at  $\gamma_b = 1.5$  and  $\gamma_s < 3$  because the two walls simultaneously confine the bubble collapse, it is still greater than at other values of  $\gamma_b$ , since the initial bubble is farther from the sidewall. At  $\gamma_s > 4.5$ , the influence of the sidewall is significantly weakened, and the velocity of an obliquely downward jet (dominated by the effect of the bottom wall) is significantly greater than that of an obliquely upward jet (dominated by the effect of buoyancy). For obliquely upward jets, the relative jet volume reaches a maximum when the jet angle is around  $45^\circ$  (at which angle the combined effect of buoyancy and the bottom wall is equivalent to the effect of the sidewall), similar to the



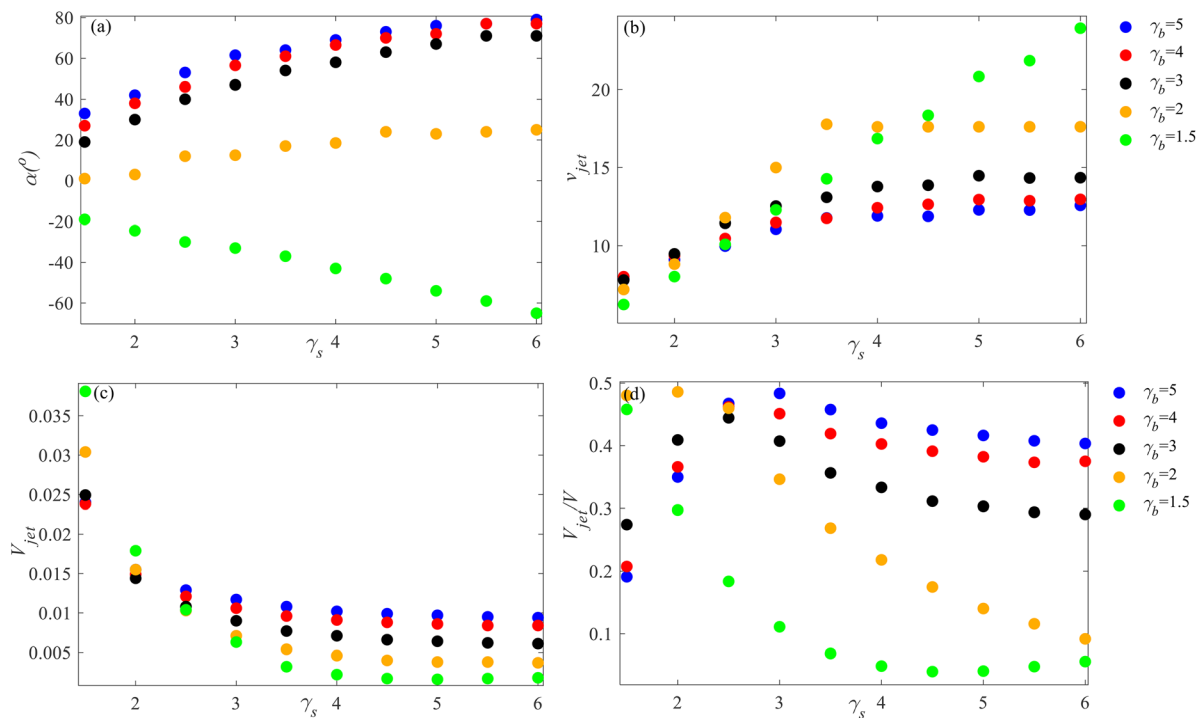


**FIG. 11.** Changes in the jet angle, velocity, volume, and relative volume with respect to  $\gamma_s$  for  $\delta = 0.2$  and  $\gamma_b = 1.5, 2, 3, 4$ , and  $5$ . (a) Jet direction. (b) Jet velocity. (c) Jet volume. (d) Relative jet volume.

case of the corner bisector for  $\delta = 0$ . When  $\gamma_b = 1.5$ , the liquid jet is inclined downward by  $45^\circ$  from the sidewall, and so an extremal value of the relative jet volume does not appear. Therefore, the maximum value of the relative jet volume occurs at larger values of  $\gamma_s$  as  $\gamma_b$  increases.

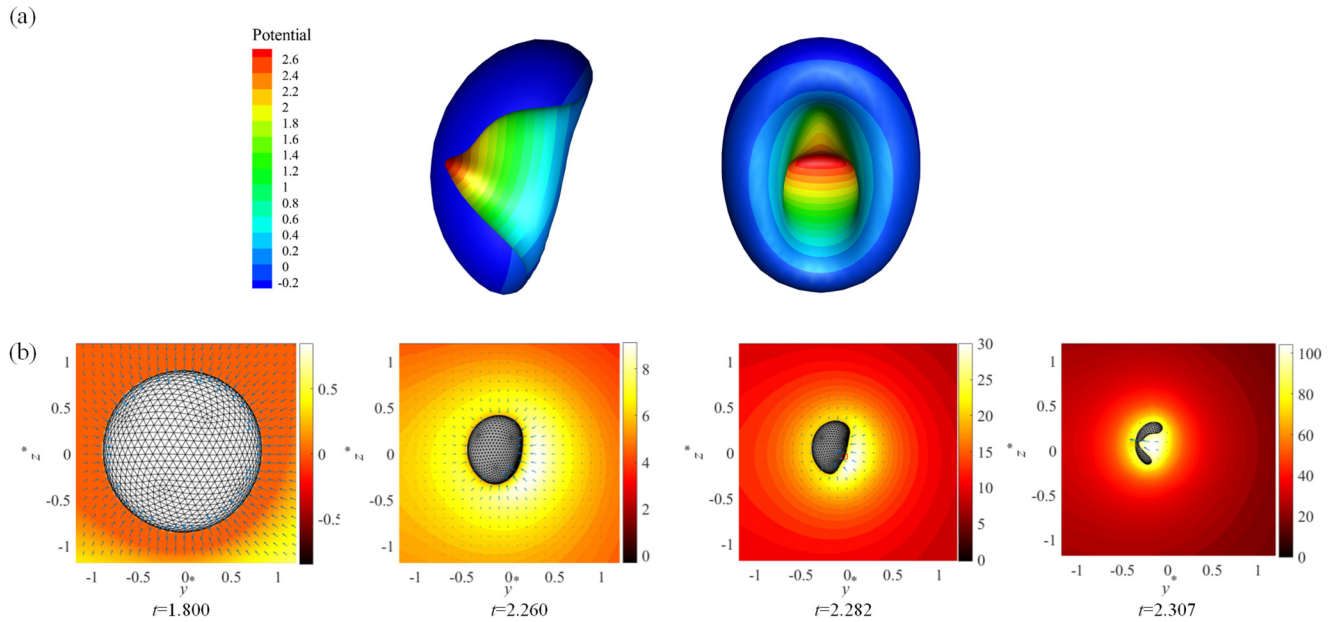
A noteworthy feature is that for  $\gamma_b = 2$ , the jet velocity remains almost constant when  $\gamma_s > 3$ , which can be explained as follows. Figure 12 shows front and side views of the jet shape at the instant of jet impact for  $\gamma_b = 2$  and  $\gamma_s = 4.5$ , together with the corresponding pressure and velocity fields at typical instants during bubble collapse. It can be seen from Fig. 8 that for  $\delta = 0.2$ , the bubble is close to the sidewall, and so the strong secondary Bjerknes force in the horizontal direction makes the bubble surface far from the sidewall entirely concave to the left. However, as the bubble is relatively distant from the sidewall, the right lower part of the bubble surface is squeezed to varying degrees during bubble collapse, resulting in a curvature reversal on the bubble surface, as can be seen at  $t = 2.282$  in Fig. 12 where the bubble surface above the small red box tends to shrink toward the left, while the fluid below the box flows obliquely upward under the action of a local high-pressure zone. Eventually, a hill-shaped liquid jet forms (the jet tip is not smooth as in Figs. 6 and 8). Because the obliquely upward movement of the liquid jet at the beginning of the bubble collapse is hindered by the inward contraction of the right bubble surface, the jet velocity does not continue to increase with  $\gamma_s$  as it does when  $\gamma_s < 3.5$ . We simulated 80 cases with different values of  $\gamma_b$  and  $\gamma_s$  in  $1.5 \leq \gamma_s \leq 6$  and  $1.5 \leq \gamma_b \leq 5$ . Only in a rectangular area ( $\gamma_s > 3$ ,  $1.5 < \gamma_b < 2.5$ ) does the hill-shaped jet occur. For  $1.5 < \gamma_b < 2.5$ , the

magnitude of the angle  $|\alpha| < 20^\circ$ , which may mean that a necessary condition for this jet pattern is that the effects of buoyancy and the bottom wall must counteract each other to a large extent. This change in jet behavior is an important reason why the Blake criterion is not applicable when the jet deviates slightly from the horizontal plane.

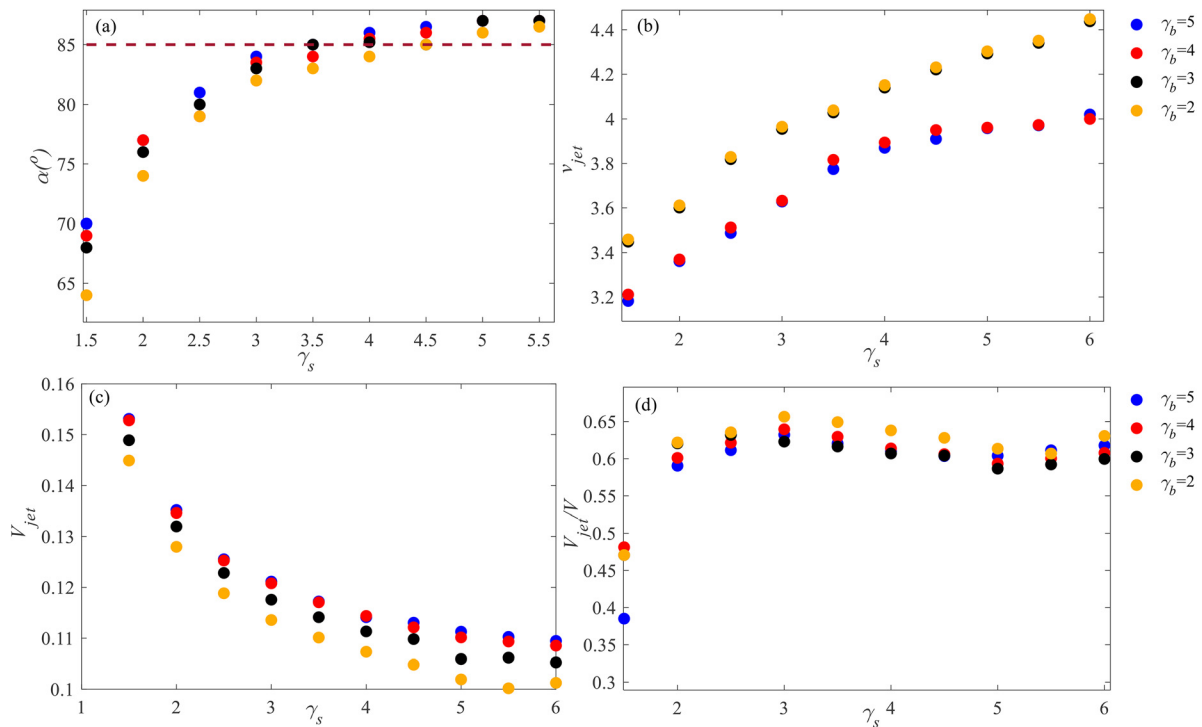
Similarly, the dependence of the jet characteristics on the distance parameters reflects the variation in the strength of the Bjerknes force. Therefore, the dependence at  $\delta = 0.2$  can be extended to cases where the effect of the bottom wall offsets that of buoyancy effect at  $\gamma_b$ . For the range of distance parameters considered in this study,  $\delta$  is between 0.073 and 0.44.

#### 4. $\delta = 0.4$ and $0.6$

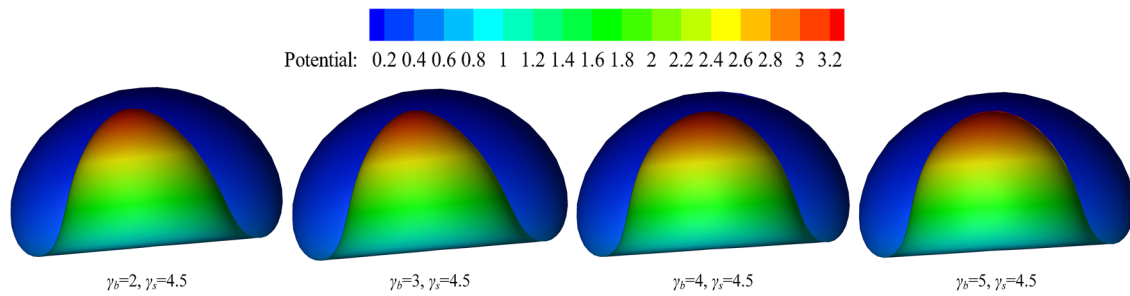
Figure 13 shows the direction, velocity, volume, and relative volume of the liquid jet for 40 cases with different values of  $\gamma_b$  and  $\gamma_s$ , for  $\delta = 0.4$  (equivalent to the bubble produced by the explosion of approximately 20 kg of TNT). For this value of  $\delta$ , since  $\gamma_b \delta > 0.44$  the effect of buoyancy on the jet characteristics dominates that of the bottom wall throughout the region under consideration. For  $\gamma_s > 4$ , the jet angle exceeds  $85^\circ$  in all cases, and thus, the jet direction is very close to the vertical, as in a free field. The jet volume decreases, and the jet velocity increases with both  $\gamma_b$  and  $\gamma_s$ . The relative jet volume is mainly stable at about 0.6, except when the effect of the sidewall is relatively strong ( $\gamma_s = 1.5$ ). The relative jet volume changes with a smaller amplitude than the cases of  $\delta = 0$  and  $0.2$ , except when the initial bubble is close to the sidewall,  $V_{jet}/V$  is relatively smaller. A rigid wall decelerates



**FIG. 12.** Jet shape and evolution of bubble collapse for  $\gamma_b = 2$  and  $\gamma_s = 3.5$ : (a) jet shape at the instant of jet impact; (b) bubble shape and corresponding pressure and velocity fields at four typical instants.



**FIG. 13.** Changes in the jet angle, velocity, volume, and relative volume with respect to  $\gamma_s$  for  $\delta = 0.4$  and  $\gamma_b = 2, 3, 4$ , and  $5$ . (a) Jet direction. (b) Jet velocity. (c) Jet volume. (d) Relative jet volume.

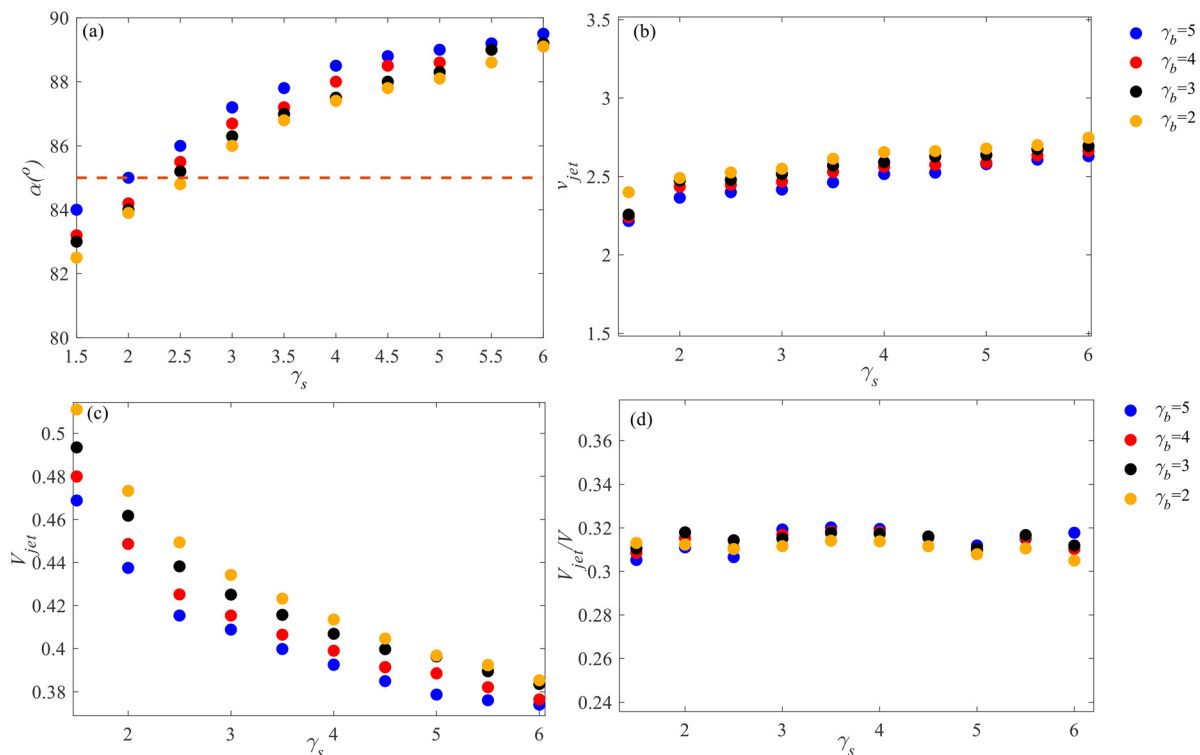

 FIG. 14. Jet shape at the instant of jet impact for  $\gamma_s = 4.5$  and  $\gamma_b = 2, 3, 4$ , and  $5$ .

the pulsation of the bubble, resulting in a bigger bubble volume and a lower jet velocity at the instant of jet impact, as well as the relatively smaller  $V_{jet}/V$ . Hence, the jet velocity increases with  $\gamma_s$ . However, it decreases with  $\gamma_b$ , since the effect of buoyancy is stronger than that of the bottom wall, which is similar to the behavior shown in Fig. 11 for obliquely upward jets. Compared with the case in which buoyancy is absent, the jet velocity at this value of  $\delta$  is significantly reduced; for example, when  $\gamma_s > 3$ , the velocity drops below 40% of that in the absence of buoyancy.

It should be noted that the jet velocities for  $\gamma_s = 2$  and  $3$  are very similar, as are those for  $\gamma_s = 4$  and  $5$ . However, the two sets of cases show clear differences. Therefore, we present a set of typical bubble shapes at the instant of jet impact for  $\gamma_s = 4.5$  and  $\gamma_b = 2, 3, 4$ , and  $5$  in

Fig. 14. The jet tip is wider at  $\gamma_b = 4$  and  $5$  than at  $\gamma_b = 2$  and  $3$ , which may cause the fluid flow at the jet tip to be relatively gentle.

Figure 15 shows the direction, velocity, volume, and relative volume of the liquid jet for 40 cases with different values of  $\gamma_b$  and  $\gamma_s$ , for  $\delta = 0.6$  (equivalent to the bubble produced by the explosion of about 200 kg of TNT). In most cases, the liquid jet tends to point almost vertically upward ( $\alpha > 85^\circ$  and  $\gamma_b \delta > 0.44$ ). Owing to the dominant effect of buoyancy on the bubble behavior, the jet volumes do not vary much, with a difference of less than 0.14 in all cases. The jet velocities are all close to 2.5, decreasing slightly with  $\gamma_b$  but increasing with  $\gamma_s$ . The relative jet volumes are stable at about 0.31. These characteristics indicate that the effect of buoyancy becomes the main factor affecting the bubble dynamics for this value of  $\delta$ . Therefore, we shall not


 FIG. 15. Changes in the jet angle, velocity, volume, and relative volume with respect to  $\gamma_s$  for  $\delta = 0.6$  and  $\gamma_b = 2, 3, 4$ , and  $5$ . (a) Jet direction. (b) Jet velocity. (c) Jet volume. (d) Relative jet volume.

consider any further cases with a stronger buoyancy effect. For  $\delta = 0.4$  and  $0.6$ , the jet velocity decreases with  $\gamma_b$  but increases with  $\gamma_s$ , and the relative jet volume varies with  $\gamma_b$  and  $\gamma_s$  within a small range. This behavior also occurs in other cases where the effect of buoyancy is stronger than that of the bottom wall throughout the region under consideration, that is, cases in which  $\gamma_b \delta > 0.44$ . For  $\gamma_b = 1.0$ , this requires that  $\delta > 0.44$ . The value  $\delta = 0.4$  is not in this range, and therefore, there is a slight error for the critical cases with  $\gamma_b$  around  $1.0$ . Finally, it should be noted again that the Blake criterion is not applicable to cases where the jet direction deviates weakly from the horizontal.

### C. Discussion of the buoyancy effect

This subsection considers eight sets of jet characteristics with fixed  $\gamma_b$  and  $\gamma_s$  for different values of  $\delta$ , as shown in Fig. 16, to examine the behavior of bubble jets with respect to buoyancy. With increasing  $\delta$ , the liquid jet rotates clockwise. A greater  $\delta$  produces a smaller difference in the jet direction over the entire area. The brown dashed line in Fig. 16(a) represents a liquid jet directed perpendicularly to the sidewall. With the exception of the region  $|\alpha| < 20^\circ$ , the product  $\delta\gamma_b$  is greater than  $0.44$  above the dashed line and less than  $0.44$  below the dashed line, which indicates that the Blake criterion<sup>37</sup> is an effective method for judging the upward or downward deflection of the liquid jet near two perpendicular walls as the jet direction deviates significantly from the horizontal.

The jet velocity first increases and then decreases with increasing  $\delta$ . For  $\delta > 0.3$ , the variation in jet velocity is significantly reduced,

with  $v_{jet}$  eventually stabilizing at a value of around  $2.2$ . As discussed in Sec. IV A, the jet velocity and bubble volume are related to the jet direction. As the jet velocity peaks, the jet angle becomes closer to zero compared with cases with other values of  $\delta$ . The jet volume gradually increases with  $\delta$  owing to the gradual increase in bubble volume during jet impact in general, with the liquid jet directed toward the sidewall with the smallest  $V_{jet}$ . The jet volume becomes larger as the bubble moves closer to the walls, because the liquid flow near the walls is confined during bubble collapse.

Because the relative jet volume represents the degree of inward depression of the bubble surface, it reflects the departure of the bubble from a spherical shape. The nonspherical collapse of a bubble is caused by the effects of buoyancy and the secondary Bjerknes force. When the effect of buoyancy is not enough to completely counteract that of the bottom wall, the effect of the secondary Bjerknes force from the walls on bubble behavior is weakened. Therefore, the relative jet volume decreases slightly with increasing buoyancy effect when  $\delta$  is between  $0$  and  $0.1$ . As the effect of buoyancy increases, it gradually overcomes the secondary Bjerknes force from the bottom wall and begins to dominate the bubble behavior, making the asymmetry of the bubble more obvious. The maximum value of  $V_{jet}/V$  occurs when  $\delta$  is about  $0.35$ . When the effect of buoyancy is pronounced ( $\delta > 0.4$ ), the relative jet volume shows a consistent downward trend with increasing  $\delta$ . When the initial bubble is relatively far from both walls, the secondary Bjerknes force is relatively weak, and hence, buoyancy has a greater effect on the nonspherical shape of the bubble. Therefore, when the initial bubble is closer to the walls, the range of variation of the relative jet volume is less.

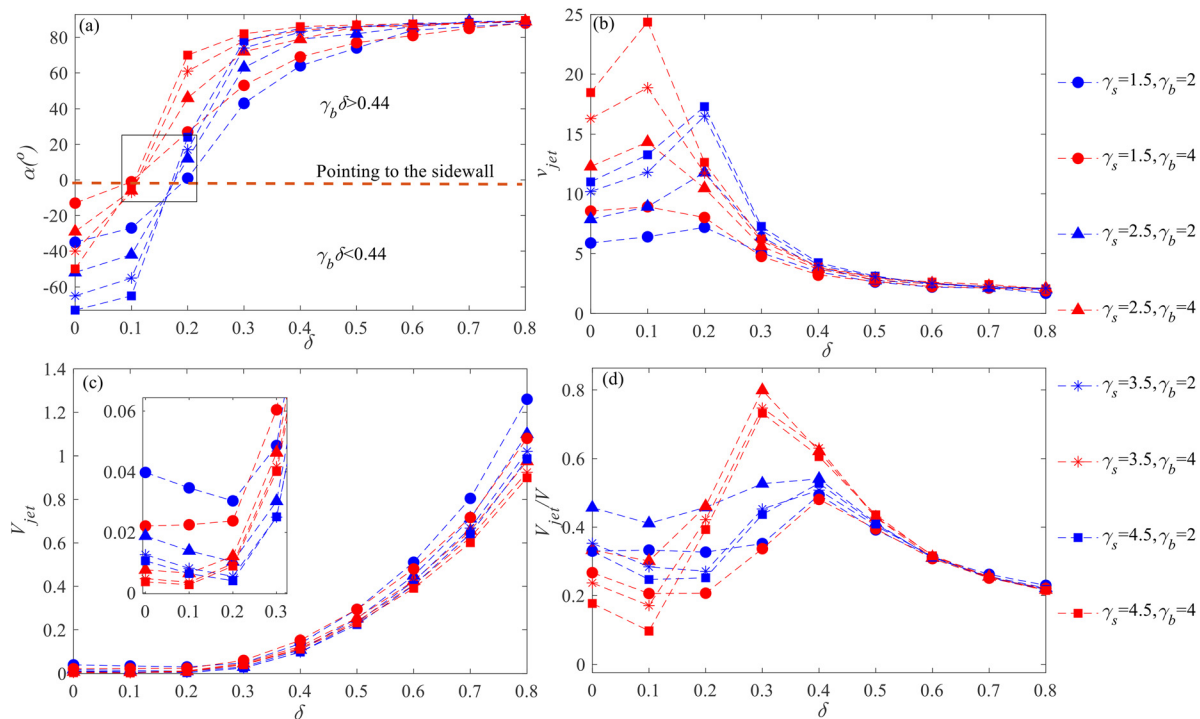


**FIG. 16.** Changes in the jet angle, velocity, volume, and relative volume with respect to  $\delta$  for different values of  $\gamma_b$  and  $\gamma_s$ . (a) Jet direction. (b) Jet velocity. (c) Jet volume. (d) Relative jet volume.



## V. SUMMARY AND CONCLUSION

In this paper, a three-dimensional boundary integral model together with the method of mirror images has been used to study buoyant pulsating bubble dynamics near a bottom wall and a vertical sidewall on the left when the bubble does not contact the walls directly in the first cycle. Numerical results show excellent agreement with the results of an underwater explosion experiment. The effect of buoyancy causes the liquid jet to rotate clockwise, which is accompanied by changes in the jet velocity (the velocity of the jet tip) and jet volume (the volume of liquid contained in the concave part of the bubble surface as the jet is about to impact the opposite bubble surface). The Kelvin impulse and a numerical technique combined with the elastic mesh velocity method have been employed to quantify the jet direction and volume. The characteristics of the bubble jet near the two walls are found to depend strongly on the buoyancy coefficient  $\delta$  and the standoff distances from the sidewall  $\gamma_s$  and the bottom wall  $\gamma_b$ .

When the jet direction deviates significantly from the horizontal plane, the Blake criterion gives reasonable predictions for obliquely upward or downward jets. The changes in jet characteristics with  $\gamma_s$  and  $\gamma_b$  exhibit three different patterns for different values of  $\delta$  based on the Blake criterion:

1. When  $\delta < 0.073$ , the bubble jet always points to the closer wall and deviates from the other wall. The jet velocity increases and the volume decreases with increases in  $\gamma_b$  and in  $\gamma_s$ . The relative jet volume first increases and then decreases with increasing  $\gamma_s$ , with a peak emerging around  $\gamma_s = 2$ .
2. When  $\delta$  is between 0.073 and 0.44, as  $\gamma_b$  increases, the liquid jet first points obliquely downward, then is directed toward the sidewall, and finally points obliquely upward, which are consequences, respectively, of the dominant effect of the bottom wall, the cancelation of the vertical Bjerknes forces, and the dominant effect of buoyancy. For smaller values of  $\gamma_b$ , the jet velocity is smaller near the sidewall and increases more rapidly with increasing  $\gamma_s$ , except when the jet deviates weakly from the horizontal. A dangerous situation for the bottom surface occurs when the initial bubble is far from the sidewall and close to the bottom: the jet is directed to the bottom with the highest velocity.
3. When  $\delta > 0.44$ , the liquid jet is directed upward and inclined to the vertical wall, and the dimensionless jet velocity increases with  $\gamma_s$  and decreases with  $\gamma_b$ . The relative jet volume varies with  $\gamma_s$  and  $\gamma_b$  over a small range.

For fixed  $\gamma_b$  and  $\gamma_s$ , the dimensionless jet velocity first increases and then decreases with increasing  $\delta$ , and finally stabilizes at a certain value. The peak of the jet velocity occurs when the jet points vertically toward the sidewall, which is dangerous for the sidewall. As  $\delta$  increases, the relative jet volume first increases and then decreases, with a local minimum at around  $\delta = 0.1$  and a peak at around  $\delta = 0.35$ .

Note that the range of  $\delta$  given above is by no means accurate, owing to the limitations of the Blake criterion, but it can provide a basic reference for the design of underwater structures. In addition, the relative magnitude of the jet load and pulsation pressure needs to be investigated profoundly using more advanced numerical methods in the future.

## ACKNOWLEDGMENTS

This work was funded by the National Natural Science Foundation of China (Nos. 51879050 and 52088102). The first author would like to express sincere thanks to Dr. Nian-Nian Liu and Dr. Ming-Kang Li for their help in experiments and Mr. Zhen-Yu Hu for communication on manuscript writing.

## REFERENCES

- <sup>1</sup>Y. Tomita and A. Shima, "Mechanisms of impulsive pressure generation and damage pit formation by bubble collapse," *J. Fluid Mech.* **169**, 535–564 (1986).
- <sup>2</sup>G. Falcucci, E. Jannelli, S. Ubertini, and S. Succi, "Direct numerical evidence of stress-induced cavitation," *J. Fluid Mech.* **728**, 362–375 (2013).
- <sup>3</sup>K. Pardeep and R. P. Saini, "Study of cavitation in hydro turbines—A review," *Renewable Sustainable Energy Rev.* **14**, 374–383 (2010).
- <sup>4</sup>T. van Terwisga, E. van Wijngaarden, J. Bosschers, and G. Kuiper, "Achievements and challenges in cavitation research on ship propellers," in *International Shipbuilding Progress* (2007), Vol. 54, p. 165.
- <sup>5</sup>J. Caldwell, "Does air-gun noise harm marine mammals?," *Leading Edge* **21**, 75–78 (2002).
- <sup>6</sup>A. Ziolkowski, G. Parkes, L. Hatton, and T. Haugland, "The signature of an air gun array: Computation from near-field measurements including interactions," *Geophysics* **47**, 1413–1421 (1982).
- <sup>7</sup>L. van Wijngaarden, "Mechanics of collapsing cavitation bubbles," *Ultrason. Sonochem.* **29**, 524–527 (2016).
- <sup>8</sup>C.-D. Ohl, M. Arora, D. Rory, V. A. Janve, and D. Lohse, "Surface cleaning from laser-induced cavitation bubbles," *Appl. Phys. Lett.* **89**, 074102 (2006).
- <sup>9</sup>E.-A. Brujan, T. Ikeda, and Y. Matsumoto, "Dynamics of ultrasound-induced cavitation bubbles in non-Newtonian liquids and near a rigid boundary," *Phys. Fluids* **16**, 2402–2410 (2004).
- <sup>10</sup>B. Dollet, W. van Hoeve, J. P. Raven, P. Marmottant, and M. Versluis, "Role of the channel geometry on the bubble pinch-off in flow-focusing devices," *Phys. Rev. Lett.* **100**, 034504 (2008).
- <sup>11</sup>S. Zhang, S.-P. Wang, A.-M. Zhang, and P. Cui, "Numerical study on motion of the air-gun bubble based on boundary integral method," *Ocean Eng.* **154**, 70–80 (2018).
- <sup>12</sup>S. Li, A. Prosperetti, and D. van der Meer, "Dynamics of a toroidal bubble on a cylinder surface with an application to geophysical exploration," *Int. J. Multiphase Flow* **129**, 103335 (2020).
- <sup>13</sup>J. J. Lyons, M. M. Haney, D. Fee, A. G. Wech, and C. F. Waythomas, "Infrasound from giant bubbles during explosive submarine eruptions," *Nat. Geosci.* **12**, 952–958 (2019).
- <sup>14</sup>J. C. Mendoza, S. Clemente, and J. C. Hernandez, "Modeling the role of marine protected areas on the recovery of shallow rocky reef ecosystem after a catastrophic submarine volcanic eruption," *Mar. Environ. Res.* **155**, 104877 (2020).
- <sup>15</sup>S. Sparks, "The dynamics of bubble formation and growth in magmas: A review and analysis," *J. Volcanol. Geotherm. Res.* **3**, 1–37 (1978).
- <sup>16</sup>J. Keller and I. I. Kolodner, "Damping of underwater explosion bubble oscillations," *J. Appl. Phys.* **27**, 1152–1161 (1956).
- <sup>17</sup>Z. Jin, C. Yin, Y. Chen, and H. Hua, "Numerical study on the interaction between underwater explosion bubble and a moveable plate with basic characteristics of a sandwich structure," *Ocean Eng.* **164**, 508–520 (2018).
- <sup>18</sup>Z.-L. Tian, Y.-L. Liu, S.-P. Wang, A.-M. Zhang, and Y.-W. Kang, "Dynamic response of floating body subjected to underwater explosion bubble and generated waves with 2D numerical model," *Comput. Model. Eng. Sci.* **118**, 397–423 (2019).
- <sup>19</sup>M. He, A.-M. Zhang, and Y.-L. Liu, "Prolonged simulation of near-free surface underwater explosion based on Eulerian finite element method," *Theor. Appl. Mech. Lett.* **10**, 16–22 (2020).
- <sup>20</sup>H. Liang, Q. Zhang, R. Long, and S. Ren, "Pulsation behavior of a bubble generated by a deep underwater explosion," *AIP Adv.* **9**, 025108 (2019).
- <sup>21</sup>J. Luo, W. Xu, and B. C. Khoo, "Stratification effect of air bubble on the shock wave from the collapse of cavitation bubble," *J. Fluid Mech.* **919**, A16 (2021).
- <sup>22</sup>N.-N. Liu, A.-M. Zhang, Y.-L. Liu, and T. Li, "Numerical analysis of the interaction of two underwater explosion bubbles using the compressible Eulerian finite-element method," *Phys. Fluids* **32**, 046107 (2020).

- <sup>23</sup>Y. Tomita and K. Sato, "Pulsed jets driven by two interacting cavitation bubbles produced at different times," *J. Fluid Mech.* **819**, 465–493 (2017).
- <sup>24</sup>G. Elisabeth, S. Thomas, and A. Arnaud, "Liquid jet eruption from hollow relaxation," *J. Fluid Mech.* **761**, 206–219 (2014).
- <sup>25</sup>W. Jiaxia, L. Kun, Y. Shijie, J. Mingzuo, and W. Zili, "Dynamics of the passive pulsation of a surface-attached air bubble subjected to a nearby oscillating spark-generated bubble," *Phys. Fluids* **32**, 067101 (2020).
- <sup>26</sup>J. Luo and Z. Niu, "Jet and shock wave from collapse of two cavitation bubbles," *Sci. Rep.* **9**, 1352 (2019).
- <sup>27</sup>Q. Zeng, S. R. Gonzalez-Avila, and C.-D. Ohl, "Splitting and jetting of cavitation bubbles in thin gaps," *J. Fluid Mech.* **896**, A28 (2020).
- <sup>28</sup>Z.-Y. Hu, Z. Cao, S. Li, and A.-M. Zhang, "Fluid-structure interaction between a high-pressure pulsating bubble and a floating structure," *Chin. J. Theor. Appl. Mech.* **53**, 944–961 (2021).
- <sup>29</sup>Y. J. Kang and C. Yeunwoo, "Gravity–capillary jet-like surface waves generated by an underwater bubble," *J. Fluid Mech.* **866**, 841–864 (2019).
- <sup>30</sup>Z. Lokar, R. Petkovsek, and M. Dular, "Cavitation bubble dynamics in a vicinity of a thin membrane wetted by different fluids," *Sci. Rep.* **11**, 3506 (2021).
- <sup>31</sup>T. Li, A.-M. Zhang, S.-P. Wang, S. Li, and W.-T. Liu, "Bubble interactions and bursting behaviors near a free surface," *Phys. Fluids* **31**, 042104 (2019).
- <sup>32</sup>A. Philipp and W. Lauterborn, "Cavitation erosion by single laser-produced bubbles," *J. Fluid Mech.* **361**, 75–116 (1998).
- <sup>33</sup>S. R. Gonzalez-Avila, D. M. Nguyen, S. Arunachalam, E. M. Domingues, H. Mishra, and C.-D. Ohl, "Mitigating cavitation erosion using biomimetic gas-trapping microtextured surfaces (GEMS)," *Sci. Adv.* **6**, eaax6192 (2020).
- <sup>34</sup>E.-A. Brujan and Y. Matsumoto, "Collapse of micrometer-sized cavitation bubbles near a rigid boundary," *Microfluid. Nanofluid.* **13**, 957–966 (2012).
- <sup>35</sup>J. R. Blake and D. C. Gibson, "Cavitation bubbles near boundaries," *Annu. Rev. Fluid Mech.* **19**, 99–123 (1987).
- <sup>36</sup>W. Lauterborn and H. Bolle, "Experimental investigations of cavitation-bubble collapse in the neighbourhood of a solid boundary," *J. Fluid Mech.* **72**, 391–399 (1975).
- <sup>37</sup>J. R. Blake, B. M. Taib, and G. Doherty, "Transient cavities near boundaries. Part 1. Rigid boundary," *J. Fluid Mech.* **170**, 479–497 (1986).
- <sup>38</sup>F. Reuter, S. R. Gonzalez-Avila, R. Mettin, and C.-D. Ohl, "Flow fields and vortex dynamics of bubbles collapsing near a solid boundary," *Phys. Rev. Fluids* **2**, 064202 (2017).
- <sup>39</sup>A. Vogel, W. Lauterborn, and R. Timm, "Optical and acoustic investigations of the dynamics of laser-produced cavitation bubbles near a solid boundary," *J. Fluid Mech.* **206**, 299–338 (1989).
- <sup>40</sup>E.-A. Brujan, G. Keen, A. Vogel, and J. R. Blake, "The final stage of the collapse of a cavitation bubble close to a rigid boundary," *Phys. Fluids* **14**, 85–92 (2002).
- <sup>41</sup>S. R. Gonzalez-Avila, F. Denner, and C.-D. Ohl, "The acoustic pressure generated by the cavitation bubble expansion and collapse near a rigid wall," *Phys. Fluids* **33**, 032118 (2021).
- <sup>42</sup>Z.-L. Tian, Y.-L. Liu, A.-M. Zhang, L. Tao, and L. Chen, "Jet development and impact load of underwater explosion bubble on solid wall," *Appl. Ocean Res.* **95**, 102013 (2020).
- <sup>43</sup>S.-M. Li, P. Cui, S. Zhang, W.-T. Liu, and Y.-X. Peng, "Experimental and numerical study on the bubble dynamics near two-connected walls with an obtuse angle," *China Ocean Eng.* **34**, 828–839 (2020).
- <sup>44</sup>E.-A. Brujan, T. Noda, A. Ishigami, T. Ogasawara, and H. Takahira, "Dynamics of laser-induced cavitation bubbles near two perpendicular rigid walls," *J. Fluid Mech.* **841**, 28–49 (2018).
- <sup>45</sup>T. Yoshiyuki and I. R. Peters, "Bubble collapse and jet formation in corner geometries," *Phys. Rev. Fluids* **3**, 081601 (2018).
- <sup>46</sup>E.-A. Brujan, T. Hiroyuki, and O. Toshiyuki, "Planar jets in collapsing cavitation bubbles," *Exp. Therm. Fluid Sci.* **101**, 48–61 (2019).
- <sup>47</sup>E. Andrews, D. F. Rivas, and I. R. Peters, "Cavity collapse near slot geometries," *J. Fluid Mech.* **901**, A29 (2020).
- <sup>48</sup>J. Cui, Z.-P. Chen, Q. Wang, T.-R. Zhou, and C. Corbett, "Experimental studies of bubble dynamics inside a corner," *Ultrason. Sonochem.* **64**, 104951 (2020).
- <sup>49</sup>S.-M. Li, A.-M. Zhang, Q. Wang, and S. Zhang, "The jet characteristics of bubbles near mixed boundaries," *Phys. Fluids* **31**, 107105 (2019).
- <sup>50</sup>S.-M. Li, A.-M. Zhang, and P. Cui, "Study on the interaction between the bubble and free surface close to a rigid wall," *Acta Aerodyn. Sin.* **38**, 796–806 (2020).
- <sup>51</sup>Y.-L. Liu, Q. Wang, S.-P. Wang, and A.-M. Zhang, "The motion of a 3D toroidal bubble and its interaction with a free surface near an inclined boundary," *Phys. Fluids* **28**, 122101 (2016).
- <sup>52</sup>E.-A. Brujan, A. Pearson, and J. R. Blake, "Pulsating, buoyant bubbles close to a rigid boundary and near the null final Kelvin impulse state," *Int. J. Multiphase Flow* **31**, 302–317 (2005).
- <sup>53</sup>A.-M. Zhang and Y.-L. Liu, "Improved three-dimensional bubble dynamics model based on boundary element method," *J. Comput. Phys.* **294**, 208–223 (2015).
- <sup>54</sup>M. Lee, E. Klaseboer, and B. C. Khoo, "On the boundary integral method for the rebounding bubble," *J. Fluid Mech.* **570**, 407–429 (2007).
- <sup>55</sup>Q. Wang, K. S. Yeo, B. C. Khoo, and K. Y. Lam, "Strong interaction between a buoyancy bubble and a free surface," *Theor. Comput. Fluid Dyn.* **8**, 73–88 (1996).
- <sup>56</sup>Q. Wang, M. Kawa, and C. Michael, "Numerical modeling of the 3D dynamics of ultrasound contrast agent microbubbles using the boundary integral method," *Phys. Fluids* **27**, 022104 (2015).
- <sup>57</sup>H. Ching-Yu, L. Cho-Chung, N. Anh-Tu, and T. Tso-Liang, "A numerical study on the underwater explosion bubble pulsation and the collapse process," *Ocean Eng.* **81**, 29–38 (2014).
- <sup>58</sup>N.-N. Liu, W.-B. Wu, A.-M. Zhang, and Y.-L. Liu, "Experimental and numerical investigation on bubble dynamics near a free surface and a circular opening of plate," *Phys. Fluids* **29**, 107102 (2017).
- <sup>59</sup>Q. Wang, M. Mahmud, J. Cui, W. R. Smith, and A. D. Walmsley, "Numerical investigation of bubble dynamics at a corner," *Phys. Fluids* **32**, 053306 (2020).
- <sup>60</sup>S. Li, R. Han, A.-M. Zhang, and Q. Wang, "Analysis of pressure field generated by a collapsing bubble," *Ocean Eng.* **117**, 22–38 (2016).
- <sup>61</sup>S. Li, D. van der Meer, A.-M. Zhang, A. Prosperetti, and D. Lohsea, "Modelling large scale airgun-bubble dynamics with highly non-spherical features," *Int. J. Multiphase Flow* **122**, 103143 (2020).
- <sup>62</sup>J. R. Blake, "The Kelvin impulse: Application to cavitation bubble dynamics," *ANZIAM J.* **30**, 127–146 (1988).
- <sup>63</sup>S. Li, B. C. Khoo, A.-M. Zhang, and S.-P. Wang, "Bubble-sphere interaction beneath a free surface," *Ocean Eng.* **169**, 469–483 (2018).
- <sup>64</sup>A.-M. Zhang, S. Li, and J. Cui, "Study on splitting of a toroidal bubble near a rigid boundary," *Phys. Fluids* **27**, 062102 (2015).
- <sup>65</sup>J. M. Brett and K. Andrew, "A study of bubble collapse pressure pulse waves from small scale underwater explosions near the water surface," *J. Sound Vib.* **435**, 91–103 (2018).
- <sup>66</sup>R. A. V. Gorder, "Dynamics of the Rayleigh–Plesset equation modelling a gas-filled bubble immersed in an incompressible fluid," *J. Fluid Mech.* **807**, 478–508 (2016).
- <sup>67</sup>K. Evert and B. C. Khoo, "A modified Rayleigh–Plesset model for a non-spherically symmetric oscillating bubble with applications to boundary integral methods," *Eng. Anal. Boundary Elem.* **30**, 59–71 (2006).
- <sup>68</sup>C. K. Turangan, G. P. Ong, E. Klaseboer, and B. C. Khoo, "Experimental and numerical study of transient bubble-elastic membrane interaction," *J. Appl. Phys.* **100**, 054910 (2006).
- <sup>69</sup>R. Cole, *Underwater Explosions* (Dover, Princeton University Press, 1948).
- <sup>70</sup>L. Rayleigh, "On the pressure developed in a liquid during the collapse of a spherical cavity," *Philos. Mag.* **34**, 94 (1917).
- <sup>71</sup>P. Cui, A.-M. Zhang, S.-P. Wang, and Y.-L. Liu, "Experimental study on interaction, shock wave emission and ice breaking of two collapsing bubbles," *J. Fluid Mech.* **897**, A25 (2020).
- <sup>72</sup>E. Klaseboer, K. Hung, C. Wang, C. W. Wang, B. C. Khoo, P. Boyce, S. Debono, and H. Charlier, "Experimental and numerical investigation of the dynamics of an underwater explosion bubble near a resilient/rigid structure," *J. Fluid Mech.* **537**, 387–413 (2005).
- <sup>73</sup>G. Song, Z.-Y. Chen, Y. Long, M.-S. Zhong, and J.-Y. Wu, "Experimental and numerical investigation of the centrifugal model for underwater explosion shock wave and bubble pulsation," *Ocean Eng.* **142**, 523–531 (2017).